A SOFT MULTIPLE- DEGREE OF FREEDOM LOAD CELL BASED ON THE HALL EFFECT

A Thesis Presented

By

QIANDONG NIE

Submitted to the Graduate School of the
University of Massachusetts Amherst in partial fulfillment
of the requirements for the degree of

MASTER OF SCIENCE IN MECHANICAL ENGINEERING

SEPTEMBER 2016

MECHANICAL AND INDUSTRIAL ENGINEERING

SOFT MULTIPLE- DEGREE OF FREEDOM LOAD CELL BASED ON THE HALL EFFECT

A Thesis Presented

By

QIANDONG NIE

Approved as to style and content by:

____

Frank C. Sup IV, Chair

____

Ian R. Grosse, Member

____

Yahya Modarres-Sadeghi, Member

____

Sundar Krishnamurty, Department of
Mechanical and Industrial
Engineering

DEDICATION

This thesis is dedicated to my loving parents Rongzhi Nie and Zhili Wu who have supported me and encouraged me since the day I was born, without them I could not be the person who I am today. I would also like to dedicate this work to my dear brother Qianchao Nie. Without him I would not have been able to finish my thesis. I also would like to thanks my friends, especially Zhi Gao, Renpeng and my brothers and sisters in the Amherst Chinese Christian Church. They have all helped me through some tough times and also shared the wonderful times with me in Amherst.

ACKNOWLEDGEMENT

I would like to thank my thesis advisor, Professor Frank Sup, for helping me with my project so patiently. He showed me what true passion and responsibility in research is. I also want to thank my lab mates, Andrew LaPre, Abhijit Kadrolkar, Haohan Zhang, Airton da Silva, Matthew Ryder, Jonathan Cummings, Vinh Nguyen, Punith Lakshmi, Mark Price and Youssef Jaber for their help and experience in getting this project off the ground.

ABSTRACT

A SOFT MULTIPLE-DEGREE-OF-FREEDOM LOAD CELL BASED ON THE HALL EFFECT

SEPTEMBER 2016

QIANDONG NIE, B.S.M.E., JILIN AGRICULTURAL UNIVERSITY

M.S.M.E., UNIVERSITY OF MASSACHUSETTS AMHERST

Directed by: Professor Frank C. Sup IV

The goal of this thesis is to develop a soft multiple-degree-of-freedom (multi-DOF) load cell that is robust and light weight for use in robotics applications to sense three axes of force and a single axis of torque. The displacement of the magnet within the elastomer changes the magnetic flux density which is sensed by two 3-axis Hall effect sensors. Experimental measurements of magnetic flux density within the area of interest were used to formulate analytic expressions that relate magnet field strength to the position of the magnet. The displacement and orientation measurement and the material properties of the elastomer are used to calibrate and calculate the applied load. The ability to measure 3-DOF force and axial torque was evaluated with combined loading applied by a robotic arm (KUKA, LBR r820 iiwa). The decoupled results show the 4-DOF load cell was able to distinguish 3-axis force and 1-axis torque with 6.9% averaged error for normal force, 4.3% and 2.6% for shear force in the X and Y axis and 8.6% for the torque. The results show good accuracy for a soft

multi-axis sensor that would be applicable in many robotic applications where high accuracy is not required.

TABLE OF CONTENTS

Page

CHAPTER

LIST OF TABLES

Table Page

LIST OF FIGURES

Figure Page

CHAPTER 1

INTRODUCTION

1.1 Overview

With the rapid developments in robotic technologies, robots have found uses in many areas, such as service (1), medical (2) (3), rehabilitation (4) entertainment (5), hazardous industries (6), etc. A robot can assist a human to complete a complicated task in various environments and needs to be equipped with many different sensors to successfully assess its environment. In the case of soft contact and flexible deformations, soft sensors have been developed for soft robotics, wearable electronic, haptic interfaces, robot manipulations, humanoid robotics, and medical robotics (7). A soft multi-degree of freedom (DOF) force sensor can be applied to increase a robot's perceptual abilities in real world. Human beings can handle objects and dexterously doing various tasks with their hands. Many parts of the dexterous manipulations depend on tactile perception in human skin. Human fingers can simultaneously feel the direction and the strength of the applied force. Therefore, it is required to develop soft sensor that can emulate human perception for sophisticated manipulation to expand utility of a soft multi-DOF force sensor. Meanwhile, a soft and high friction surface with high deformation sensor can also be applied on robotic finger tips or artificial palms, which would allow a robotic hand to hold unknown objects more steadily and provides a safer cushion to protect the robotic hand._However, common multi-DOF force and torque sensors typically are rigid physical structures and are costly to fabricate as well.

The specific performance and fabrication method of a multi-DOF force depends on the transduction method of the sensor. The fabrication method can be simplified by decreasing the number of sensing elements. However, traditional sensing elements such as piezoresistivity, capacitance and piezoelectricity only measure a single DOF, which requires multiple elements to measure multiple DOFs. In this thesis, coupled approach is taken and a 4-DOF load cell is designed to measure normal stress, shear stress and torsion simultaneously using only one magnet suspended within an elastomer above two 3-axis Hall effect sensors.

1.2 Research Scope

This research combines finite element methods, solid mechanics, nonlinear optimization algorithm simulation, and mechatronics principles to realize a soft multi-DOF load cell. The goal of this work is to design a soft, robust 4-DOF load cell using inexpensive and simple fabrication procedures. This is accomplished with a magnet localization method which uses the magnetic flux density measured by 3-axis Hall sensor to calculate the position of the magnet relative to the sensors. The real analytic expression of magnetic flux density around a magnet is hard to define, a calibration method is discussed in this thesis using a genetic algorithm software, EUREQA, to find equations that fit a 3D dataset. Additionally, the axial rotation about the magnet is determined by a mathematic model using the 2D local position of two 3-axis sensors related to magnet via MATLAB, a numerical computing software.

The design is detailed to outline the determination of magnet, sensor and elastomer, which is guided by simulation of magnetic flux density around a magnet. The evaluation work is composed of three parts. First, the localization method of magnet is evaluated on a 3-axis stage. Secondly, single degree of freedom (DOF) performance of prototype sensor is accomplished on tensile test machine (Instron machine 4411) with normal and shear stress test. Finally, a real time 4-DOF performance of the prototype sensor is evaluated using a robotic arm to apply a combined loading conditions on to the sensor.

It is important to understand that this thesis is to investigate a new idea to achieve a soft 4- DOF load cell without deep discussion on specifics of sensors. The design of prototype sensor does not suggest that selection of magnet, elastomer and Hall effect sensor in this thesis is the best choice, however, it serves as a guide to determine the necessary characteristics for all the components in the senor. Finally, the actual data from the robotic arm is a referential criterion to evaluate the sensor's 4-DOF measuring ability, which reveals the performance of the prototype sensor fulfill the goal in this thesis.

1.3 Thesis Outline

This thesis is organized into seven chapters. CHAPTER 1 is the introduction which discussed research motivation and goals in this thesis. CHAPTER 2 discusses the background work which presents overview of some traditional force sensors along with fundamental knowledge on the Hall effect and its applications in sensing. In addition, an analytic expression of a distributed magnetic field around a rectangular magnet is reviewed. CHAPTER 3 presents a localization tracking method of magnet is developed via EUREQA and run in the MATLAB. CHAPER 4 presents the prototype design and steps through the selection of magnet, elastomer and Hall effect sensor. CHAPTER 5 presents the evaluation methods and results of the 4-DOF load cell in single axis loading and under combined loads. CHAPTER 6 concludes with the contributions of this thesis along future works.

CHAPTER 2

BACKGROUND

2.1 Soft Sensor

The development of soft sensor has been of interesting for decades. By the end of 1970 tactile sensing was recognized as a field of study that had the potential to address many engineering problems associated with robotic manipulation. Many types of tactile sensor were designed and developed in 1980s (8), and research mainly focused on sensors and materials which could mimic the response of mechanoreceptors in the human skin (9) (10). To date, most of the tactile sensors developed for robots only measure normal contact force on the sensor surface. However, for the dexterous manipulation of objects, the detection of shear force is as important as the detection of normal force, particularly for slip detection (11). Recently, some soft sensors could measure both normal stress and shear stress simultaneously. Most popular multiple tactile sensor are based on transduction technique of piezoresistive (12) (13) or strain gauges (14) (15), which are restricted by high quantity of sensing elements and are prone to be affected by temperature (16). Hyung-Kew Lee developed a tactile sensor with embedded multiple capacitors, which is insensitive to temperature change and could simultaneously measure normal and shear stress. However, the sensor is composed of arrays of pressure transducers whose fabrication was not simple enough (16). In order to decrease the cost of raw components, a compact sensor with a sample physical structure is necessary to consider about. Daniel M. Vogt developed a soft multi-axis force sensor which own a relative simple structure by using embedded microfluidic channels. However, the loading capacity and resolution is limited and it had a problem of nonlinear response (17). Asuka Kadowaki developed a multi-axis tactile sensor which is constructed by molding a soft urethane foam with infrared LEDs and corresponding phototransistors (18). The soft tactile sensor is able to detect 3-dimensional deformation so that some characteristic contact patterns including stroking, pinching and pushing is available to be discriminated. However, the sensor could not provide a linear performance and the accuracy is limited. The existing commercial six degree of freedom (DOF) force/ torque sensors are too expensive and often over designed for robot research (19).

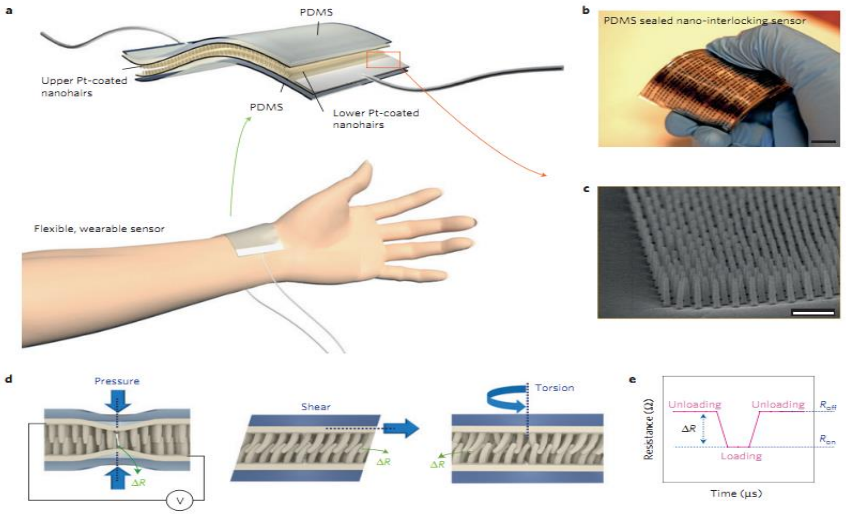

Figure 2.1: Multiplex, flexible strain-gauge sensor based on the reversible interlocking of Pt-coated polymer nanofibres (20).

In Figure 2.1, a flexible and highly sensitive strain-gauge sensor is composed of two interlocked arrays of high-aspect-ratio Pt-coated polymeric nanofibres that are supported on thin polydimethylsiloxane layers, which could distinguish a normal, shear or torsional load (20). However, the structure of the device is not easy to fabricated and there is no clear resolution of force and torque and other specifics about the sensor.

To overcome the limitation of high deformation, thermal affection, multi-dimensional, a magnetic type tactile sensor has been developed recently. The transducer presented in Figure

2.2 measures the resistance of semiconductor resistor which varies with the strength of the magnetic field it is in. The transducer used is a three-DOF force sensor with a low profile (4.9 mm× 16mm diameter) which is developed to investigate the combination of both normal and shear stress during gait motion for improving its prosthetic fit (21). However, the transducer includes many peripheral circuits such as amplifier, filter, A/D convertor which is hardware intensive and an offline data processing is also needed. Hiroyuki Nakamoto proposed a magnetic type tactile sensor (22) which also has a simple structure with an elastic layer and a substrate layer applied on a gripper, as shown in the Figure 2.3, the sensor is proposed to measure 3-axes of displacement and force. However, at least four Giant magnetoresistance (GMR) elements are used for fabrication. The max error of each axis is large as 0.2 N over full range 1 N. Therefore, a multi-axis magnetic sensing elements, 3-axis Hall effect sensor is investigated in the next section.

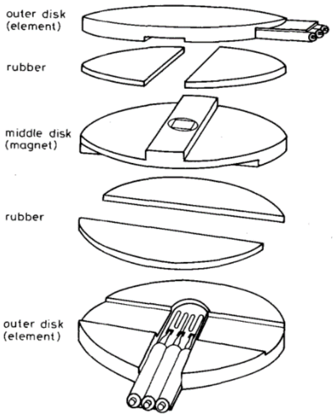

Figure 2.2: Exploded assembly of the biaxial shear transducer (21)

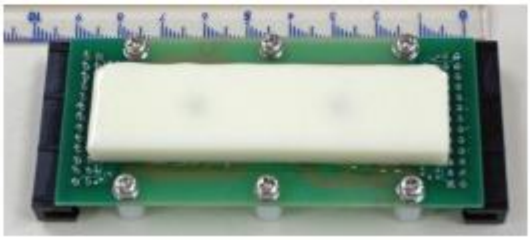

(a) Upper surface

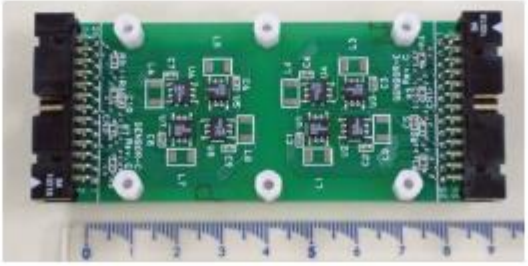

(b) Buttom of substrate

Figure 2.3: The tactile sensor can measure 3 DOF force and 3 DOF displacement (22)

2.2 Hall effect based on sensor

The Hall effect is a produced from a semi-conductor with an electric current flowing through it in presence of a magnetic field. As shown in Figure 2.4, a transverse force, the Lorentz force, on the charging carriers is exerted by magnetic field which trends to push them to one side of the semi-conductor. A measurable Hall voltage between the two sides of semi-conductor is produced when the buildup charge balances the magnetic influence, which was discovered by E. H. Hall in 1879 (23). Therefore, a Hall effect sensor requires a magnetic field to activate the device. However, the Hall voltage potential across the Hall element is so minuscule that it may easily be affected by outside forces such as temperature and package stresses (24). Hall effect technology was not widely applied until low-cost integrated circuit were developed in 1980s. More recent devices are able to amplify the signal, in addition to application of the utilization of on-chip, offset cancellation techniques, which have allowed

Hall effect sensing technology to be employed even under extreme environmental conditions (24).

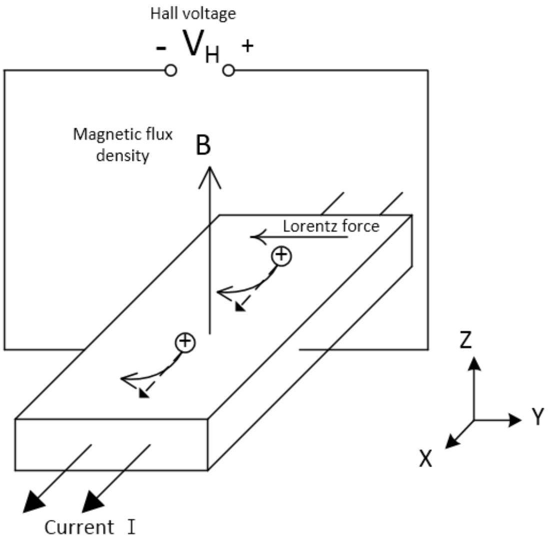

Figure 2.4: Theoretical principle of Hall Effect

A common linear Hall effect sensor can be used for position and motion sensing. When a magnet gets close to an object, its position, displacement and angular sensing are possible. Compared with other methods for position or motion sensing such as optical and electromechanical sensing, Hall effect devices are immune to dust, dirt, mud and water. The "non-contacting" feature of Hall effect sensor makes it possible a longer lifetime.

The triaxis Hall effect technology is accomplished by adding a structured ferromagnetic layer at the surface of die, which is able to detect magnetic fields parallel to the surface of integrated circuit (IC). Commercial 3-axis Hall effect sensors are available. Their characteristics include immunity to temperature change, small package. 3-axis Hall effect sensor can typically be used as 3-axis spatial locating sensor such as 3D joystick. In this project, two 3-axis Hall effect are used to determine orientation of a magnet in order to calculate three-axes of force and a sinlge-axis moment.

As depicted in Figure 2.5, Ledermann presented a conventional capacitive tactile sensor only detects one variable-capacitance node. As the two right pictures shown in Figure 2.5, only one variable-capacitance node is not enough to determine the orientation of load. Therefore, in practice a capacitive tactile sensor has to be composed of an array of capacitive elements to determine a combined load. Similarly, sensing elements like strain gauges and piezoelectric elements are also one dimension variables, multiple force and moment sensors based on those elements have to determine a complex structure to locate an array of sensing elements as presented in (25) and (26).

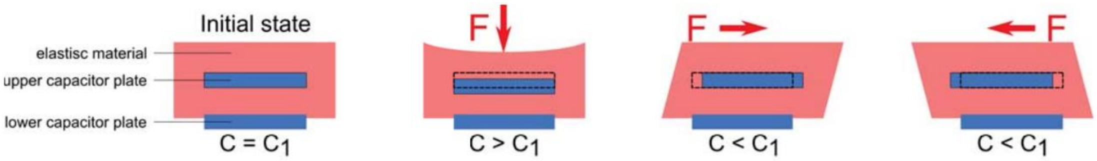

Figure 2.5: Working principle of a conventional capacitive tactile sensor (27)

In comparison, a magnetic field is a 3D spatial source with three components of the magnetic density flux exists to be detected at a point. A 3-axis Hall effect sensor which is fixed on site relative to a magnet can detect the movement of the magnet by measuring the change in the magnetic field. A 3-axis Hall sensor detects three components simultaneously providing three independent variables to determine the deformation of loading medium and the movement of magnet which is presented in the Figure 2.6.

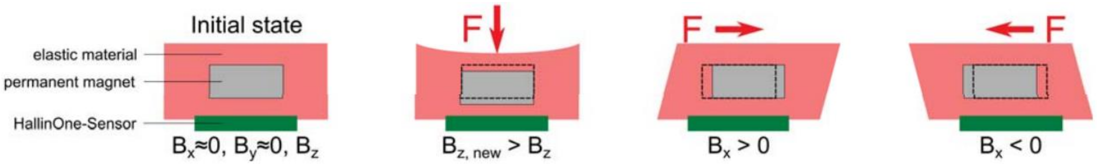

Figure 2.6: Working principle of Hall effect tactile sensor (27)

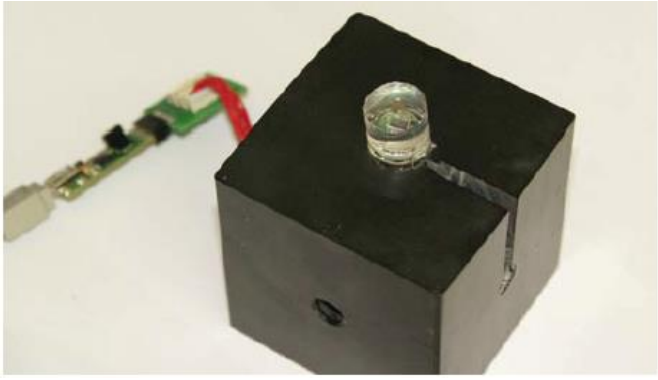

Figure 2.7: Tactile sensor based on one 3D Hall sensor (27)

In Figure 2.7 shows a prototype of tactile sensor which is just based on a single 3D Hall sensor (27) whose digital data from the 3D Hall sensor is easy to access. All the peripheral circuits are integrated in a tiny 3D Hall sensor(5.0 mm X 6.4mm) leading an easy way to fabricate the tactile sensor, but it only measures one degree of freedom of force which is limited to be applied in robotic area.

Tomo developed a three-axis Hall-Effect based skin sensor which was shown in Figure 2.8: The prototype of the Hall effect-based skin sensor shown in Figure 2.8. The prototype has a very simple physic structure and could detect three axis force simultaneously while maintaining a soft exterior for safe interactions. However, the sensor cannot measure any torque and has limited loading capacity, which only tested for a total force of 0.7 N to 14 N in the normal and tangential directions of the prototype sensor (28). A linear and a quadratic regression model with Robust Huber regression (MATLAB function LinerModel.fit) and neural network results in different R-square values in Table 2.1.

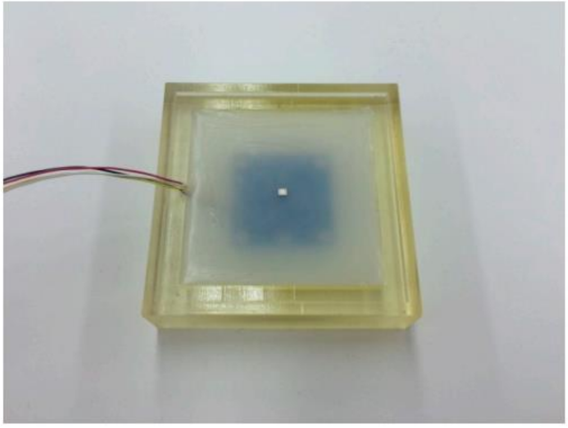

Figure 2.8: The prototype of the Hall effect-based skin sensor (28)

Table 2.1 : R-Square value for normal and shear force experiment for the Hall effect-based sensor (28)

	Linear + Huber	Quadratic + Huber	Feedforward Neural Network
Normal Force	0.8634	0.8925	0.9368
Shear 45 - y	0.8634	0.9418	0.8275
Shear 45 - x	0.9272	0.9744	0.9644

In this thesis, a multi-DOF force and moment sensor based on the Hall effect is proposed. Like the tactile sensor presented in (28), the multi-DOF force and moment sensor also houses a magnet but uses two 3D Hall effect sensors. A prototype is fabricated as simple as the sensor shown in Figure 2.8. The new sensor can measure 3-axis force and one axis torque simultaneously with a peak loading higher than done in (33).

2.3 Analytic expression of magnetic flux density

In order to determine displacement and orientation of magnet within elastomer, an expression for the distribution of magnetic flux density around a permanent magnet is necessary to be determined. According to the molecular current model, an analytic expression exactly describing the magnetic field distribution of rectangular permanent magnets was derived from the Biot–Savart's law and is presented in (29). The reason to choose a rectangular magnet instead of a cylindrical magnet is discussed in the Chapter 4. As shown in Figure 2.9, a rectangular magnet in length *L*, width *W* and height *H* locates in a local coordinate system (*O', X', Y', Z'*), and its body is in saturation state with symmetrically magnetizing along *Z'* axis. So magnetic flux density at an arbitrary point P (*a', b', c'*) around the rectangular magnet is expressed as:

$$B' = B_x' i + B_y' j + B_z' k \qquad (1).$$

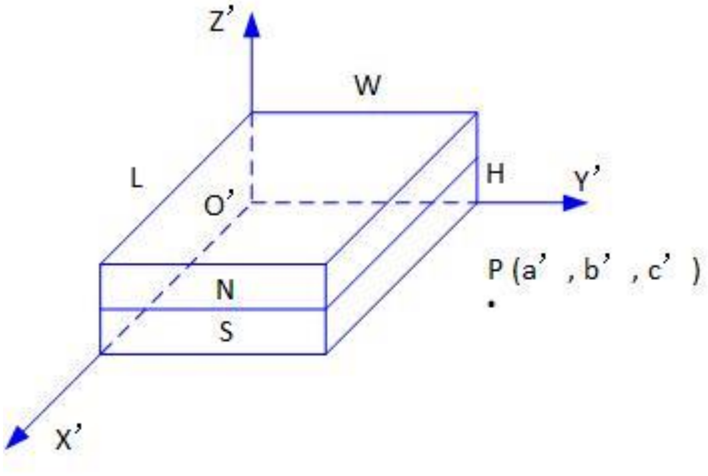

Figure 2.9: A rectangular magnet in a local coordinate system (30)

The three orthogonal components of the magnetic flux are presented in Eqns. (2), (3), and (4). In these Eqns. (2), (3), (4), there are two sub-functions Γ and Φ, which are shown in Eqns. (5) and (6). According to these Eqns., the magnetic flux density at any arbitrary point

(a', b', c') around a rectangular magnet of a known size can be determined. Relative parameters are presented in the Table 1.

$$B'_x = -\frac{k}{2}\left[\Gamma(L-a',b',c')+\Gamma(L-a',W-b',c')-\Gamma(a',b',c')-\Gamma(a',W-b',c')\right]\Big|_0^H \tag{2}$$

$$B'_y = -\frac{k}{2}\left[\Gamma(W-b',a',c')+\Gamma(W-b',L-a',c')-\Gamma(b',a',c')-\Gamma(b',L-a',c')\right]\Big|_0^H \tag{3}$$

$$B'_z = -K\begin{bmatrix}\Phi(b',L-a',c')+\Phi(W-b',L-a',c')+\Phi(a',W-b',c') \\ +\Phi(L-a',W-b',c')+\Phi(W-b',a',c')+\Phi(b',a',c') \\ +\Phi(L-a',b',c')+\Phi(a',b',c')\end{bmatrix}\Bigg|_0^H \tag{4}$$

B'_x, B'_y, B'_z	Three components of magnetic field in local coordinate system
a', b', c'	The position of arbitrary point P' in Local coordinate system
L, W, H	The dimension of the rectangular magnet
K	A constant depends on the very magnet, $k = (\mu_0 J)/4\pi$
Γ, Φ	Two sub-functions are shown in (5), (6)
μ_0	Air magnetic permeability (T*m/A)
J	The current density on any plane which is parallel to the plane X'O'Y'
$[\bullet]\Big\|_0^H$	The difference of function in the bracket when z= H and z =

Table 2.2: Description of parameters in expressions (2) (3) (4)

And two functions Γ , Φ are:

$$\Gamma(r_1, r_2, r_3) = \ln \frac{\sqrt{r_1^2 + r_2^2 + (r_3 - z_0)^2} - r_2}{\sqrt{r_1^2 + r_2^2 + (r_3 - z_0)^2} + r_2} \tag{5}$$

$$\Phi(\phi_1, \phi_2, \phi_3) = \tan^{-1}\left[\frac{\phi_1}{\phi_2} \frac{(\phi_3 - z_0)}{\sqrt{\phi_1^2 + \phi_2^2 + (\phi_3 - z_0)^2}}\right] \tag{6}$$

Observation from Eqn. (2)-(3) show, three component of magnetic flux density B_x, B_y and B_z consist of two sub-equations (5) and (6), which is very complicated to solve these transcendental equations to know the movement and orientation of magnet. A six-dimensional magnetic localization algorithm for rectangular magnet objective based on a particle swarm optimizer introduced in (30), which is sensitive to initial guess and expensive in computing time. This problem is solved by using EUREQA in the next chapter, which formulate two set of analytic expressions of displacement and orientation of magnet based on a 3D dataset around a rectangular magnet. The physical relationship present by analytic expressions in Eqn. 2-6 is used to setup a target expression to be satisfied while searching for a formula, which is setup in the user-specified building blocks in the EUREQA. This formula building- blocks are consisted of a range of operators such as arithmetic, trigonometric, inverse trigonometric, exponential, etc.

CHAPTER 3

APPROACH

As shown in Figure 3.1, the soft concept is composed of a magnet embedded in an elastomer and suspended over two 3-axis Hall effect sensors. In this chapter, the method for calculating the applied load on the top surface of load cell is presented. First, a localization method is presented to determine the displacement and orientation of the magnet over the two 3-axis Hall effect sensors. To do this experimental measurements of magnetic flux density on $17 \times 17 \times 4$ data point grid were collected to formulate analytic expressions that relate the magnetic field strength to the position of the magnet using EUREQA. Next, the rotation about Z axis is calculated by a mathematic model of the displacement magnet relative to each of the two sensors. Finally, a linear calibration model is present based on the 3D solid mechanics equations to calculate the applied load.

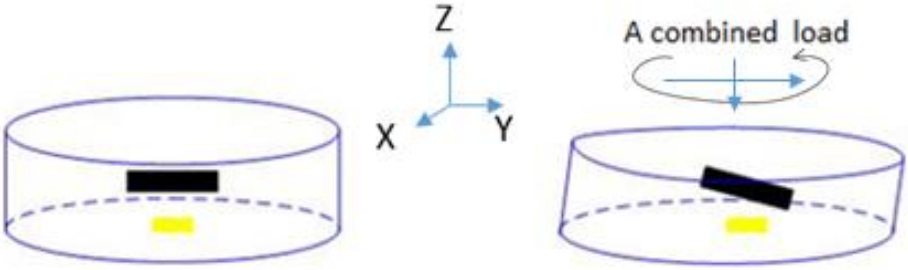

Figure 3.1: The movement of magnet (the black block) in the deformed elastomer is tracked by two 3-axis Hall sensors (the yellow block)

3.1 Localization method of magnet

In this project, the displacements of magnet in X, Y and Z axis is calculated by analytics expressions solved by EUREQA. Two sets of analytic expressions are present in the Appendix. The first expression set reveals relation between displacement of the magnet and all the six variables B_{x1}, B_{y1}, B_{z1}, B_{x2}, B_{y2}, B_{z2}, the target expression is shown in Eqns. (7) – (9) below:

$$X = F_1 (B_{x1}, B_{y1,} B_{z1}, B_{x2}, B_{y2,} B_{z2}) \quad (7)$$

$$Y = F_2 (B_{x1}, B_{y1,} B_{z1}, B_{x2}, B_{y2,} B_{z2}) \quad (8)$$

$$Z = F_3 (B_{x1}, B_{y1,} B_{z1}, B_{x2}, B_{y2,} B_{z2}) \quad (9)$$

The second analytic expression set is solved using EUREQA starting with the six target expressions as shown in Eqns. (10) – (15), which means position of magnet is measured by each sensor simultaneously. Displacement of magnet can be determined using the averaged result from the two sensors. The first set of analytic expressions have a higher coefficient of determination (R-Square) than the second one as shown in appendix, because the expressions are derived from the dataset of both two sensor, which has double quantity of parameters than the second set does. The first set of analytic expressions is used as calibration of magnet's displacement in the single DOF prototype evaluation in the Chapter 5 because of the higher accuracy.

$$X_1 = F_4 (B_{x1}, B_{y1,} B_{z1}) \quad (10)$$

$$Y_1 = F_5 (B_{x1}, B_{y1,} B_{z1}) \quad (11)$$

$$Z_1 = F_6 (B_{x1}, B_{y1,} B_{z1}) \quad (12)$$

$$X_2 = F_7 (B_{x2}, B_{y2,} B_{z2}) \quad (13)$$

$$Y_2 = F_8 (B_{x2}, B_{y2,} B_{z2}) \quad (14)$$

$$Z_2 = F_9 (B_{x2}, B_{y2,} B_{z2}) \quad (15)$$

The data collection work was accomplished on a 3-axis micrometers as shown in Figure 3.2. Measurement of magnetic flux density is collected within a cubical space in 5.08 mm × 5.08 mm × 2.00 mm by assuming that the magnet stays within this same volume in the physical prototype during loading.

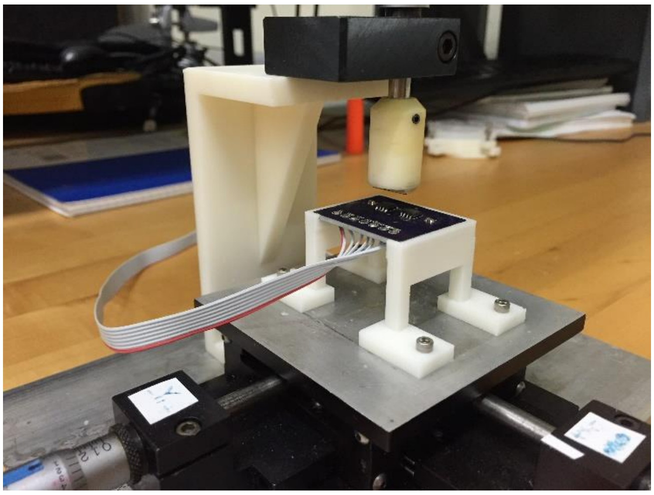

Figure 3.2: Micrometer for data collection

Next, γ, the angle of rotation on Z axis, is determined by a mathematic model. Firstly, two coordinate systems are set as shown in Figure 3.3, which are local coordinate system (O', X', Y', Z') and global coordinate system (O, X, Y, Z). In the global coordinate system, one corner of a rectangular magnet in the size of length (L), wide (W) and height (H) locates at $(\mathrm{x}_0, \mathrm{y}_0, \mathrm{z}_0)$. The corner point is exact the original point O' in the local coordinate system. The local coordinate axes are fixed with three edges of magnet which as shown in as shown in Figure 3.3. A coordinate transformation is shown by translation matrix T and rotation matrix R which is shown as

$$(\mathrm{a}, \mathrm{b}, \mathrm{c}, 1) = (a', b', c', 1) * T * R \tag{16}$$

$$\mathrm{T} = \begin{bmatrix} 1 & 0 & 0 & 0 \\ 0 & 1 & 0 & 0 \\ 0 & 0 & 1 & 0 \\ -x_0 & -y_0 & -z_0 & 1 \end{bmatrix}$$

$$\mathrm{R} = \begin{bmatrix} \cos\alpha\cos\gamma + \sin\alpha\sin\beta\sin\gamma & \cos\gamma\sin\alpha\sin\beta - \cos\alpha\beta\sin\gamma & \cos\beta\sin\alpha & 0 \\ \cos\beta\sin\alpha & \cos\beta\cos\gamma & -\sin\beta & 0 \\ \cos\alpha\sin\beta\sin\gamma - \cos\gamma\sin\alpha & \sin\alpha\sin\gamma + \cos\alpha\cos\beta\sin\gamma & \cos\alpha\cos\beta & 0 \\ 0 & 0 & 0 & 1 \end{bmatrix}$$

After a translation and a rotation of the magnet has occurred in the local coordinate system, the location of an arbitrary point *P (a', b', c')* is expressed in Eqns. (17), (18) and (19). The parameters in the equations are defined in Table 3.1. The local position of the two 3-axis sensors are determined by a second set of analytic expressions solved for via EUREQA, which is substituted into Eqns. (17), (18) and (19). According to vector rotation transformation, the actual measurement of magnetic flux density of sensor in the local coordinate system is present in Eqn. (23).

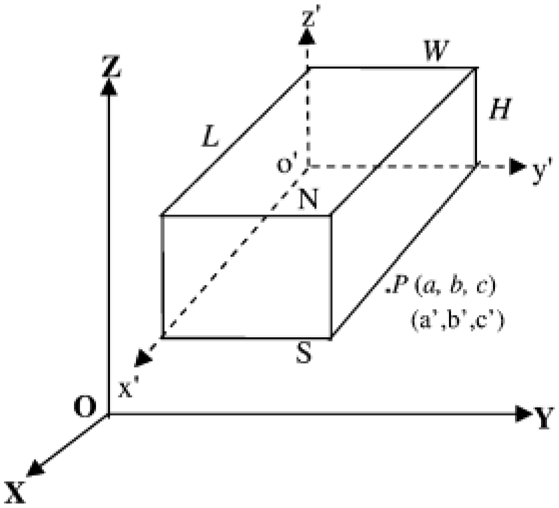

Figure 3.3: Global and local coordinate system (30).

To solve the least-square-error problem as shown in Eqn. 20, a nonlinear optimization method is applied. The six parameters X, Y, Z, α, β and γ can be calculated by the least-squares error nonlinear function "lsqnonlin" in the MATLAB. The iterative function is implemented with an initial guess of six parameters, which is set as all zero. An upper boundaries and a lower boundaries are set as ± 2.54 mm for translation in the X, Y and Z axis and ±20 degree for rotation about three axes. In this project, data from sensor is proposed to send to PC's COM Port with a UART cable. For a safe and clean data transferring, a sample time 0.2 was set up for loading test in the Chapter 5. Only γ is proposed to be determined by solving the least-square-error problem which assumes only rotation along the Z axis. In prior work it was noted that the rotation angle is sensitive to the initial guess (30). Therefore, selecting an accurate initial guess plays an important role in solving a solution here. It is important to understand that the first set of analytic expressions would not work when a significant rotation occurs. Therefore, the displacement of magnet is only determined by the second set of analytic expressions during a real time prototype evaluation under combined loading shown in Chapter 5.

$$a' = \cos(\alpha)\cos(\gamma)(a-x_0) - \sin(\alpha)(c-z_0) + \cos(\alpha)\sin(\gamma)(b-y_0) \tag{17}$$

$$\begin{aligned} b' = {} & (\cos\beta\cos\gamma + \sin\alpha\sin\beta\,\mathrm{sind}\gamma(b-y_0) - (\cos\beta\sin\gamma - \cos\gamma\sin\alpha\sin\beta(a-x_0) \\ & + \cos\alpha\sin\beta(c-z_0) \end{aligned} \tag{18}$$

$$\begin{aligned} c' = {} & (\sin\beta\sin\gamma + \cos\beta\cos\gamma\sin\alpha)(a-x_0) - (\cos\gamma\sin\beta - \cos\beta\sin\alpha\sin\gamma)(b-y_0) \\ & + \cos\alpha\cos\beta(c-z_0) \end{aligned} \tag{19}$$

$$\mathrm{B} = \mathrm{B}' * R^{-1} \tag{20}$$

Table 3.1: Parameter definitions for Equations (17) (18) (19).

a, b, c	Position of point p in the global coordinate system
a', b', c'	Position of point p in the local coordinate system
x_0, y_0, z_0	Original of the local coordinate system
α, β, γ	Euler angle of rotation of its local coordinate $Y'X'Z'$ axes in accordance with global coordinate axe Y, X, Z

3.2 Loading model

Solid mechanics theory is used to determine the relationship between the load applied to the surface of an elastomer and the movement of the magnet within the elastomer. Assuming the elastomer is isotropic and elastic, the stresses (normal and shear stress) on the loading surface displace the magnet and change its orientation and position. From Hooke's Law, the normal stress σ is linear proportional with the normal strain ε, which is shown in Eqn. 21. The normal stress is the result of force applied to a surface. The normal strain is the extension over the original length. The shear stress τ is also linear proportional with shear strain γ, which is shown in Eqn. 22 below.

$$\varepsilon = \frac{\sigma}{E} \tag{21}$$

$$\gamma = \frac{\tau}{G} \tag{22}$$

The shear stress is the result of force over a certain surface, and the shear strain is defined as the change in angle. Two constants *E* and *G* are Young's modulus and shear modulus, respectively, which are mechanical properties of the material. When a torsion is applied on Z-axis (axially), the orientation and position of magnet change. In order to detect the combined load simultaneously, the deflection caused by load and moment is assumed to be the sum of effects caused by the each loading separately using the principle of superposition. The principle of superposition is known as the effect (stress, strain, or deflection) produced on an elastic system by any final state of loading is the same whether the forces that constitute that loading are applied simultaneously or in any given sequence and is the result of the effects that the several force would produce if each acted independently (31). In this project, elastomer was assumed to have a linear behavior.

Applying Hooke's Law in three dimensions, the combined strain ε_{zz} is presented in Eqn. 23 and shear strains are present in Eqns. 24 and 25. However, only normal stress occurs in the Z axis on the sensor in this project as shown in Figure 3.1, so normal stress is actually calculated by Eqns. 27 and 28 in this project. As shown in Eqn. 27, a normal stress applied in the Z axis is proportional to elastomer's displacement in the Z axis. The result of displacement of elastomer in the Z axis, D_{e_z}, over height of the elastomer, H_e, which is proportional to the displacement of the magnet in the Z axis, D_{mgt_z}, which is determined by Eqn. 28. The shear stresses, τ_{zy} and τ_{zx}, applied on the sensor shown in Figure 3.1 is calculated in Eqns. 29- 32, which is also proportional to elastomer's displacement in the X and Y axis as presented in Eqns. 30 and 32. In expression (26), the torsion, *T*, is expressed by single variable angle, θ, with torsion constant, shear modulus, and length, *L*.

$$\varepsilon_{zz} = -\frac{v\sigma_{xx}}{E} - \frac{v\sigma_{yy}}{E} + \frac{\sigma_{zz}}{E} \tag{23}$$

$$\gamma_{zx} = \frac{\tau_{zx}}{G} \tag{24}$$

$$\gamma_{zy} = \frac{\tau_{zy}}{G} \tag{25}$$

$$\mathrm{T} = \frac{J_T}{L} G\theta \tag{26}$$

$$\sigma_{zz} = E * \frac{D_{e\_z}}{H_e} \tag{27}$$

$$D_{e\_z} = \frac{D_{mgt\_z}}{H_{mgt}} * H_e \tag{28}$$

$$\tau_{zy} = G * \frac{D_{e\_y}}{H_e} \tag{29}$$

$$D_{e\_y} = \frac{D_{mgt\_y}}{H_{mgt}} * H_e \tag{30}$$

$$\tau_{zx} = G * \frac{D_{e\_x}}{H_e} \tag{31}$$

$$D_{e\_x} = \frac{D_{mgt\_x}}{H_{mgt}} * H_e \tag{32}$$

Combined displacement and orientation of magnet determined by the localization method of magnet in the section 3.1 with the assumed linear material property discussed in solid mechanics above, a calibration method was developed during the prototype sensor evaluation in Chapter 5 *Result.*

CHAPTER 4

SENSOR DESIGN

The soft 4-DOF load cell is composed of three main elements: the 3D Hall sensors, a magnet and an elastomer. The magnet is embedded in the elastomer and two 3D Hall sensors are located at the bottom of elastomer as shown in Figure 4.1. The resolution and loading capacity of 4-DOF load cell can be adjusted based on the selection of the magnet, elastomer, resolution of Hall Effect sensors, and the overall geometric parameters of the device, all of which can be selected by the designer. In this chapter, the fabrication process, the magnet parameterization, Hall effect sensor performance relating to sensor design, and guidelines for selection of the elastomer are presented.

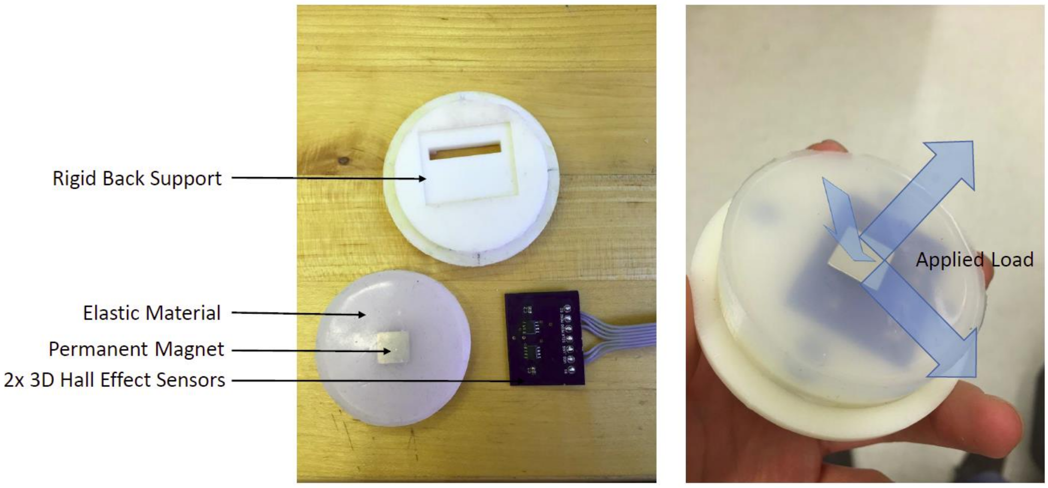

Figure 4.1: The prototype of multi-axis soft load cell.

4.1 Prototype design

The prototype sensor is fabricated using two part elastomer casting process using the following steps. First, a rigid back support is 3D printed to hold the printed circuit board (PCB) that holds the two 3-axis Hall effect sensors. Next the elastomer is cast in two layers. The first layer is made for 0.15 inch with a magnet shaped stick inserted in the center of elastomer layer. Before casting the second layer, the magnet is placed in the prefabricated cavity. Finally, the elastomer poured on top of the first layer, which results in a total height of 0.35 inch for the prototype sensor. To ensure good bonding to the back support an elastomer adhesive is applied on the some contacting places between the top back support and bottom silicone when all the curing work finished.

In order to obtain a unique and larger change in magnetic flux density, the sensor is located at the point where the change in magnetic flux density is highest and within working range of sensor. The closing the distance between the magnet and the sensor maximizes the change magnetic flux density. The thinnest gap was designed as 0.15 inch for protecting sensor from a collision with magnet by large applied loads and to allow for displacement of the magnet to measure normal loads. The sensors and magnet are located in the elastomer as Figure 4.2 shown.

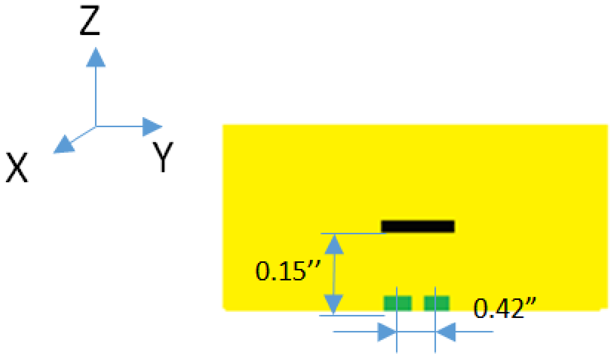

Figure 4.2: The magnet embedded in the elastomer above the two 3D Hall effect sensors.

4.2 Magnet Selection

This sensor is based on changes in magnetic field due to the relative orientation and position of sensor relative to the magnet. The choice of magnet is critical to maximize the sensing range of the 3D Hall effect sensor. The magnetic flux density radiating from the magnet is measured by the 3-axis Hall effect sensor while magnet moves during loading. Therefore, features of the magnet like strength, shape, dimensions and magnetization direction directly affect the performance of the load cell. The digital output of 3D Hall sensor is proportional to the magnitude of magnetic flux density B which is determined by those features of magnet and the distance from the magnet. In this project, the magnet selected was a made of neodymium grade N42 and size 0.5 inch × 0.25 inch × 0.0625 inch (B841, K&J Magnetics, Inc.). The details of how this magnet was selected are detailed in this section.

4.2.1 Magnet Shape

Magnets typically come in rectangular or cylinder/disc shapes and either axially or diametrically magnetized. Magnetic density maps are shown in Figure 4.3 for disc and block (rectangle and square) magnets in axially and radially magnetized directions. The magnetic flux density around the magnet in simulated in COMSOL Multiphysics, which is a general-purpose FEA software platform based on advanced numerical methods for modeling and simulating physics-based problems (32). The AC/DC Module from the COMSOL is used here for simulating magnetic field around a stationary permanent magnet.

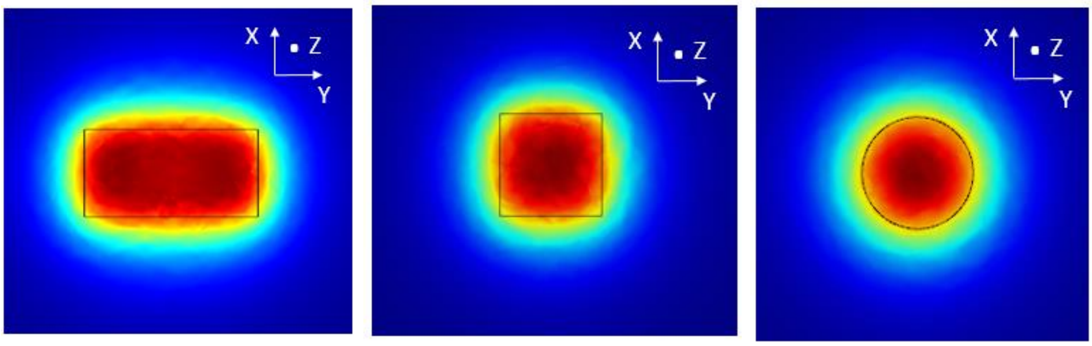

(a) rectangular magnet (b) square magnet (c) Disc magnet

Figure 4.3: Magnetic flux density map simulated in COMSOL

The Figure 4.3(a) presents norm of magnetic flux density on X-Y plane which is 0.2 inch away from the surface of a rectangular magnet. The disc magnet as shown in Figure 4.3(c) reveals the radially symmetric field not result in any change on magnetic flux density when a rotation occurs. However, comparing Figure 4.3(a) and Figure 4.3(b), the gradient of magnetic flux density along X and Y axes are different which results in a continuous and smooth change in magnetic flux density when rotated. To determine the shape of magnet as rectangle or square, the magnetic flux density curves of two kinds of magnet were simulated in Figure 4.4. The rectangular magnet (0.50 inch X 0.25 inch) and square magnet (0.50 inch X 0.50 inch) are both N42 neodymium magnets. As shown in the Figure 4.4, both square and rectangular magnet make a significant change in Y-axis of the field while a rotation of magnet occurs in the axis Z from 1/16 π to -1/16 π over a sensor along located along the long axis of magnet. As Figure 4.4 (a) shows, the variance of B_y is up to 370 G for the rectangular magnet, but only 170 G for the square magnet in Figure 4.4 (b) . It is a clear demonstration that halving the size rectangular magnet linearly decreases B_y. To obtain more significant changes in the magnetic flux density while rotating about the Z-axis, a rectangular magnet axially magnetized is preferred.

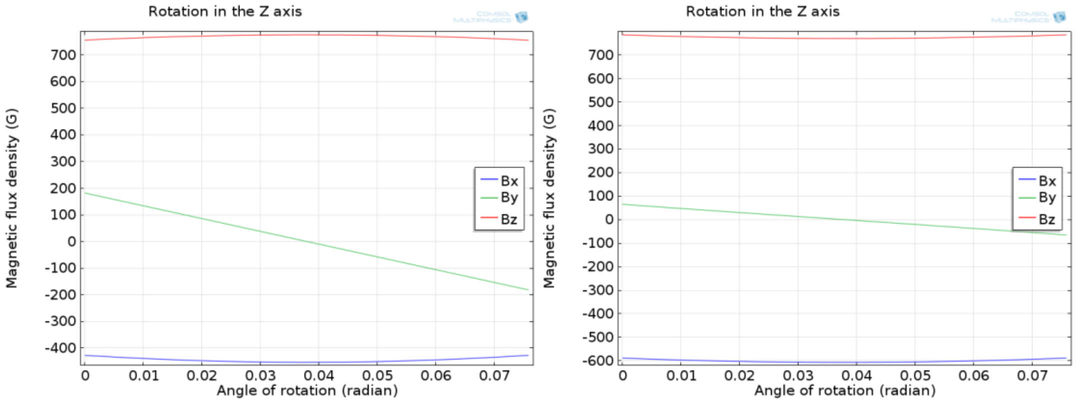

(a) (b)

Figure 4.4: Simulated Magnetic flux density while rotating a (a) square and (b) rectangular magnet.

4.2.2 Magnet Size and Orientation with respect to Hall Effect Sensor

The dimensional ratio of magnet affects the magnetic field distribution significantly. In order to determine tendency of variance on B_y while Z axis rotation for length to width the ratio, regular ratio of dimension on commercial magnet around 1/2 such as 3/4 and 1/3 was selected to simulate for Z-axis rotation in the COMSOL. Comparing with 1/2, whose magnetic flux density curve was presented in the Figure 4.5 above, a lower ratio of 1/3 as shown in Figure 4.5 (b) indicated a larger variance of 420 G on By is obtained, which results in a lower dimensional ratio of the magnet and a larger change in magnetic flux density for Z-axis rotations.

Considering a sensor located along the short axis of a magnet. The same rotation occurs on a magnet of radio 0.5 whose magnetic flux density curve is presented in the Figure 4.6 and presents two sensing sites on the Y axis (not on the X axis as simulated above). Figure 4.6 (a) showed the data curve while the sensor is located at 0.1” in the Y axis, which is within the short length of magnet. Figure 4.6 (b) present data curve while the sensor is located at 0.15” in the Y axis, which is beyond the short length of magnet. From observation of Figure 4.6 show, a lower variance on B_y obtained. Therefore, the two sensors should be located along the axis aligned with longer length of magnet.

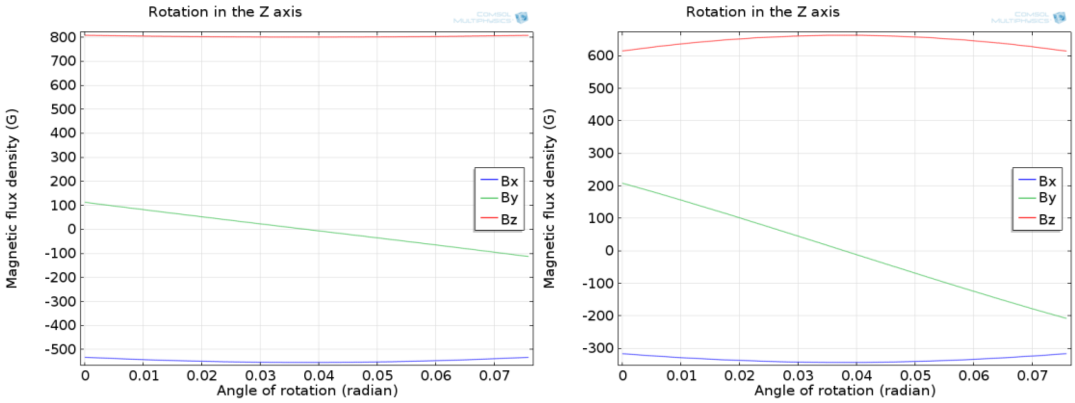

(a) (b)

Figure 4.5: Simulation of magnetic flex density for rotation around a magnet with a length to width ratios of length over width for (a) 3/4 and (b) 1/3.

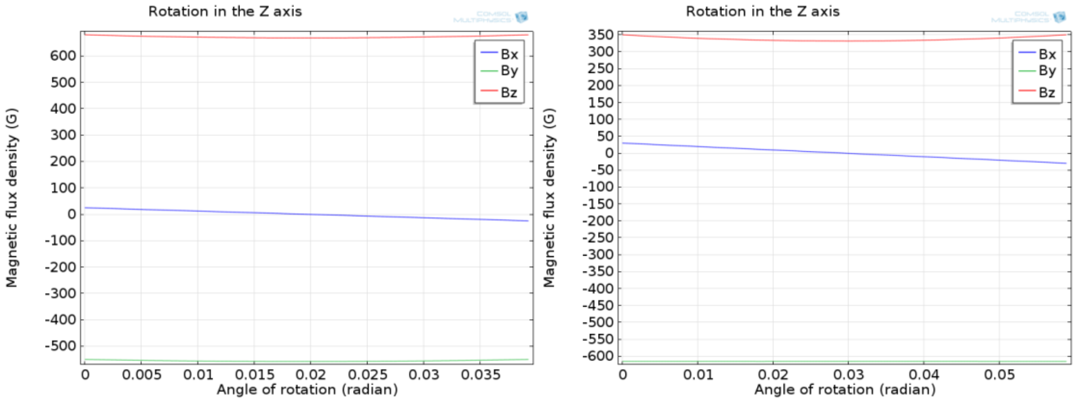

(a)Sensor at close location in the Y axis (b) Sensor at far location in the Y axis

Figure 4.6: Simulation of magnetic flex density for rotation around a magnet with length to width ratio 0.5 over sensor located along short axis of magnet at location of 0.1” and 0.15”.

The 4-DOF load cell in this project not only depends on Z-axis rotation resulting from an applied torque about the Z-axis, but also changes in the magnetic flux density during 3-axis translation to measure three components of force. In order to obtain a higher resolution for the prototype, an appropriate magnet located at certain sensing point, where results in a larger average variance of magnet flux density upon certain translation is considered here. To determine an appropriate dimensional ratio during certain translation in the X, Y and Z axis, all the three components of magnetic flux density curve for different dimensional ratio of rectangular magnet are shown in Figure 4.7. The largest average variance of absolute magnetic flux density on X axis translation is about 420 G for a ratio of 1/2 as shown in Figure 4.7. The largest average variance of absolute magnetic flux density on Y axis translation is about 405 G for a ratio of 1/2 as shown in Figure 4.8. The largest average variance of absolute magnetic flux density on the Z axis translation is about 315 G for a ratio of 1/2 as shown in Figure 4.9. Therefore, the appropriate dimensional ratio of a rectangular magnet was determined to be 1/2 to maximize resolution in all 4-DOFs.

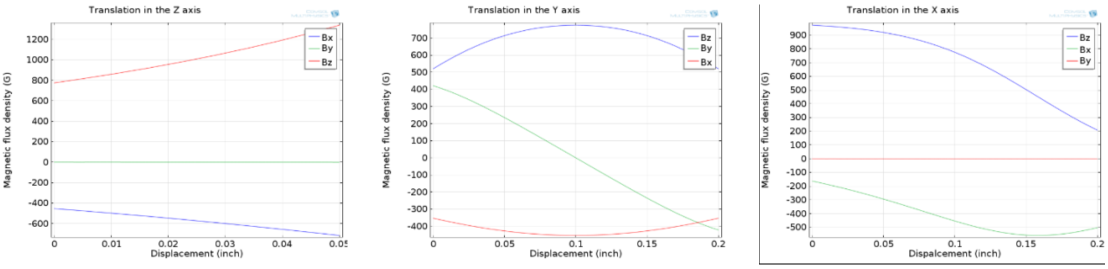

(a) Translation in the Z axis (b) Translation in the Y axis (c) Translation in the X axis

Figure 4.7: Simulation of magnetic flex density for three axes while translating across a rectangular magnet with length over width ratio of 1/2 in the Z, Y, and X axes.

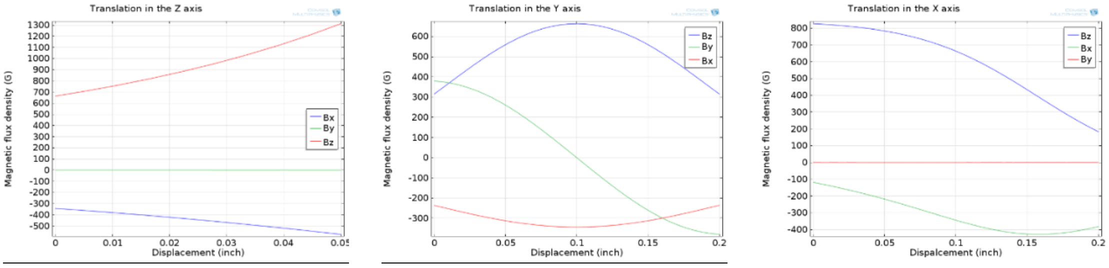

(a) Translation in the Z axis (b) Translation in Y axis (c) Translation in the X axis

Figure 4.8: Simulation of magnetic flex density for three axes while translating across a rectangular magnet with length over width ratio of 1/3 in the Z, Y, and X axes.

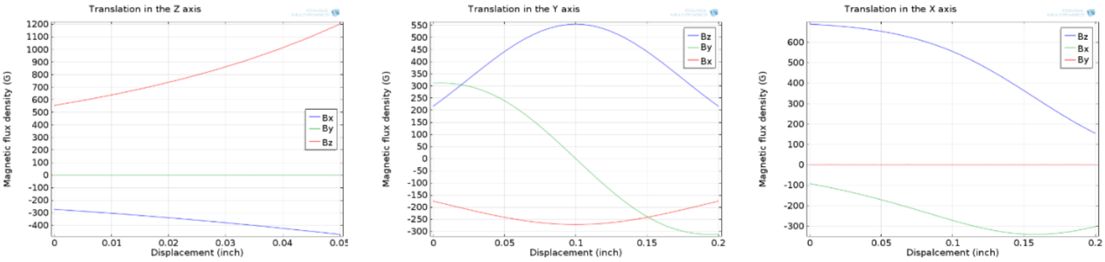

(a) Translation in the Z axis (b) Translation in the Y axis (c) Translation in the X axis

Figure 4.9: Magnetic flux variance for three axes while translating across a rectangular magnet with length over width ratio of 1/4 in the Z, Y, and X axes.

Even though dimensional ratio of magnet has been determined, the physical dimensions of the magnet also affects the package of prototype design and magnetic flux density surrounding the magnet as well. To improve the resolution of the sensor and keep the magnet as small as possible, an appropriate dimensional ratio of the magnet is important. It also aids in placement of the two 3-axis Hall effect sensors so they are located where steepest gradient of magnetic flux density occurs during X-Y-Z axis translation and Z-axis rotation. An additional simulation was built with two 3-axis Hall effect sensors located at (-0.25 inch, 0 inch, -0.15 inch) and (0.25 inch, 0 inch, -0.15 inch). A magnet (0.50 inch × 0.25 inch ×0.063 inch) was used. Shown in Figure 4.10, the magnetic flux density curve for X axis translation is presented. The distance of translation is twice the length of the magnet, which is 1.0 inch. In Figure 4.10, the steepest gradient of the B_x curve is from 0.3 inch to 0.4 inch and the steepest gradient of the B_z curve is from 0.2 inch to 0.3 inch. The gradient of the B_y curve is supposed to be zero as sensor is located in the X axis. Therefore, one sensor in negative X axis prefer to be placed between -0.3 inch and -0.1 inch where distance between two sensors is from 0.2 inch up to 0.6 inch, which is between 40% and 120% of long length of magnet. Sensors located within this range results in best resolution during translation occurs in the X axis, which means best resolution could be obtained for shear force in the X axis. In order to obtain high resolution during translation in the Y axis and Z axis, two more set of simulation is present in Figure 4.11 and Figure 4.12.

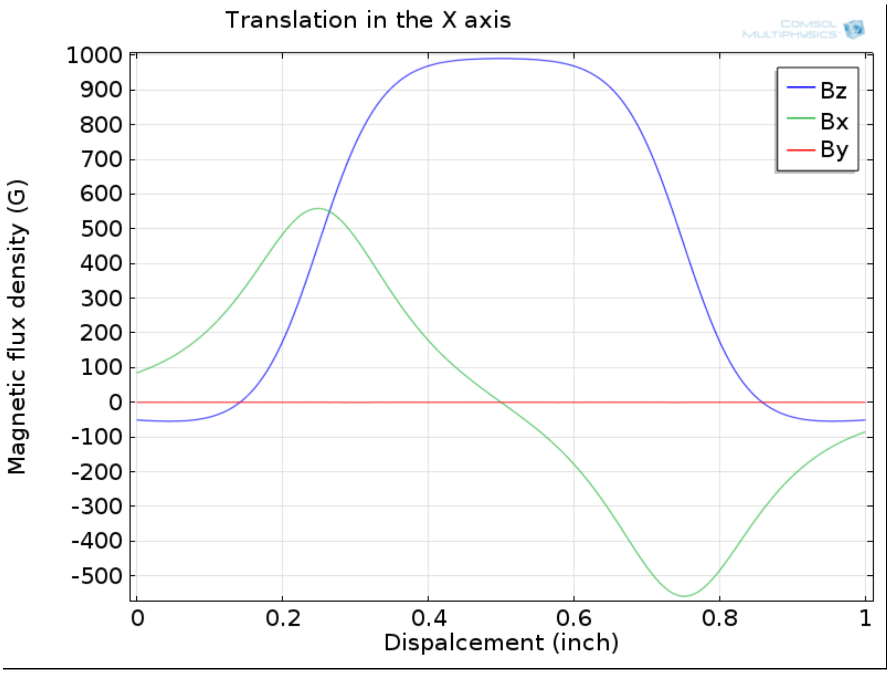

Figure 4.10: Three axes magnetic flux density curve during X axis translation.

In Figure 4.11 and Figure 4.12, the translation on the Y and Z axis was measured by placing the sensor at incremental positions of -0.1 inch, -0.25 inch, -0.4 inch and -0.6 inch along the X axis, which is 20%, 50%, 80% and 120% of the length of the magnet. The position on Y axis was fixed at 0 inch and -0.15 inches for the Z axis. In Figure 4.11, the B_z varies more than the others where the sensor is placed at -0.4 inch in the X axis (80% of the length of the magnet). In Figure 4.12, the data from the location at -0.4 inch shows large variances as well except in B_y when a translation occurs on the Y axis as shown in Figure 4.12(b). However, for obtaining larger gradients on all the three magnetic components B_x, By, Bz, the most appropriate location site of sensing element is near the 80% position over the magnet, which is ± 0.3 inch on X axis. Due to the packaging of the 3-axis Hall effect sensor (Melexis, MLX 90363), the minimum distance between the two sensing sites should be at least 0.25 inch. Considering a smallest dimension of the magnet, the length of magnet is determined to be 0.50 inch and the width is 0.25 inch.

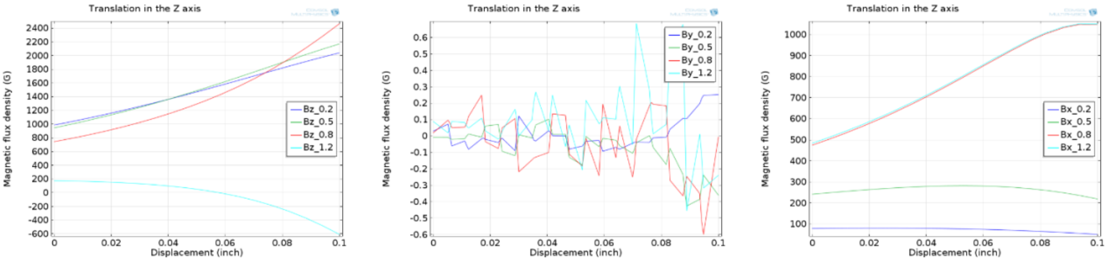

(a) B_z (b) B_y (c) B_x

Figure 4.11: The variance curves of magnetic flux density at selected sensing positions during translation on Z axis.

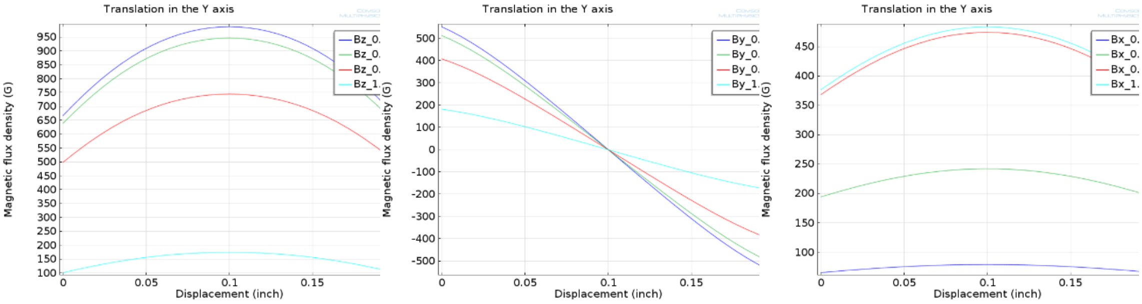

(a) B_z (b) B_y (c) B_x

Figure 4.12: The variance curves of magnetic flux density at selected sensing positions during translation on Y axis.

4.2.3 Magnet Strength Selection

In order to achieve a maximize resolution of the sensor with a low profile and compact size, the magnitude of gradient of magnetic flux density around magnet along all axis could be increased by using a strong magnet. Because a stronger magnet produces a larger magnetic flux density than a lower grade magnet of the same size. Neodymium magnets are the strongest type of permanent magnet commercially available (33). In Figure 4.13, the three components of the magnetic flux density at the sensing location (0.2 inch, 0 inch, -3.81 inch) for a grade N42 and N52 magnets were simulated during Z axis translation from -0.15 inch to -0.05 inch. The magnitude of B_x, B_y and B_z produced by N52 is 200 G higher than N42 during 0.10 inches of translation on the Z axis but almost same at the starting point. Therefore, the magnet in grade of N42 is strong enough in this project for fabricating a preliminary prototype load cell. It is important to understand here the magnetic flux density produced by a very strong magnet might exceed the limitation of sensor, which means the loading capacity would be decreased at the same time. Therefore, the selection of magnet really depends on the specifics of the measurement application, which is not discussed in this thesis.

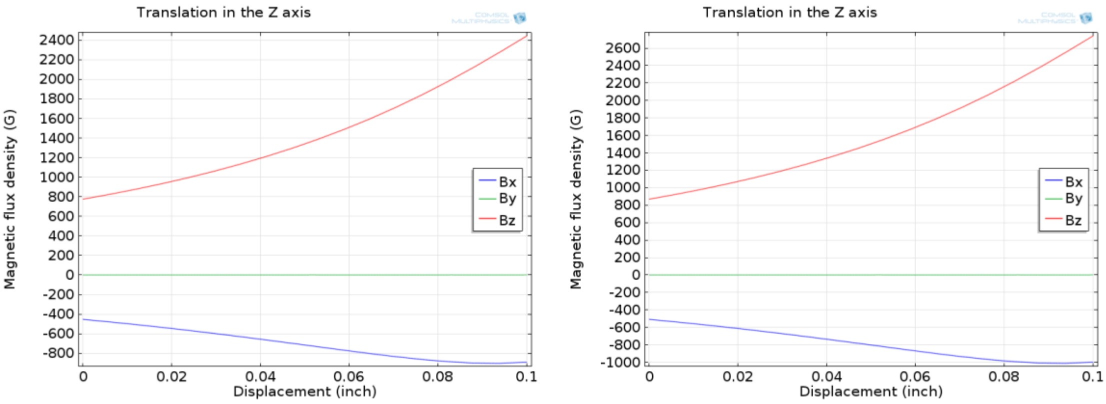

(a)N42 magnet

(b) N52 magnet

Figure 4.13: Three magnetic flux density versus translation along the Z axis for two magnet strengths.

4.3 Hall Effect Sensor Selection

The readout of the Hall effect sensor is converted into load magnitude through the approach discussed in the Chapter 3. Therefore, a 3D Hall effect sensor with high digital resolution in a small size is preferred here because it provides three high resolution sensing data, which results in higher resolution load cell. Additionally, a fast data transfer protocol is required to maximize sample rate.

In this project, all three components of magnetic flux density are used. In order to simplify the fabrication of prototype sensor, two 3-axis Hall effect sensors are used. Melexis developed a ferromagnetic layer called the integrated magneto concentrator (IMC), which is a key technology to achieve a 3-axis Hall effect sensor integrated chip. In this project, the sensor MLX 90363 by Melexis is used. The MLX90363 by Melexis which is a 3D Hall effect sensor with a wide measurement range of up to 700 mT and uses the high speed serial peripheral interface (SPI compatible – full duplex). It has 14 bit output resolution and is compact (6.4 mm X 4.9 mm), which is good enough to be used in this project. It is important to understand that the main goal in this thesis is to bring out an idea to build a soft 4-DOF load cell based on Hall effect. Several rules for selecting a Hall effect sensor above is a guidance pointing to a relative appropriate senor but not the best one. In the future, the latest sensor MLX 90393 from Melexis is proposed to used, which owns higher 16 bit resolution and a more compact size (3 mm × 3 mm).

4.4 Elastomer Selection

The performance of the 4-DOF load cell is dependent on the mechanical properties of the elastomer used. A softer material increases resolution, however larger deformations decrease the measuring range. . It also should be flexible which means having a good recover property and low hysteresis as well. In this project, cast silicone (Dragon Skin FX PRO) is chosen as the initial candidate elastomer because of its low modulus (37.8 psi for the first 100 % strain) and is robust. In addition, the curing time of dragon silicone is only 30 minutes, which allowed for quick and convenient prototyping. Additional advantages like good flexibility, wide range of hardness and high load bearing capacity make it a reasonable elastomer. The material properties of the silicone elastomer used are shown in Table 4.1. However, what should be understood here that it may not be the ideal material and detailed elastomer selection criteria is outside the scope of this thesis

Table 4.1: Technical review of Dragon Skin Fx Pro

Cure time: 40 minutes (73°F / 23℃)
Color: Translucent
Shore A Hardness: 2
100 % Modulus, psi: 228

CHAPTER 5

EVALUATION

5.1 Evaluation of localization method of magnet

The magnet's movement and orientation is determined by a tracking method detailed in the Chapter 3. In order to evaluate the accuracy of the tracking method independent of the elastomer a 3-axis micrometer stage shown in the Figure 5.1 was used. The X and Y axis displacements are measured with manual micrometers. A digital encoder (AMT 103) was fixed on the Z axis to measure the rotation of magnet. The magnet was moved within a 0.197" × 0.197" × 0.079" volume.

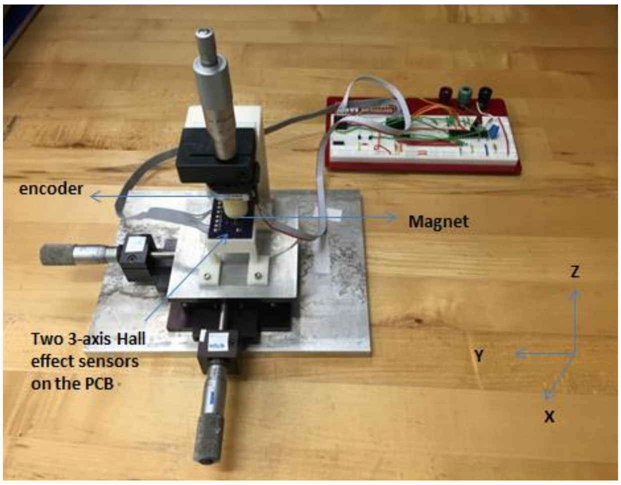

Figure 5.1: 3-axis micrometer stage equipped with the encoder AMT103-V

The accuracy of the localization method to determine the magnet position relative to the sensors is presented in Figure 5.2 to Figure 5.5. Figure 5.2 (a) shows the magnet moving from -0.10 inch to +0.10 inch on X axis while fixing the Y and Z axes and no rotation on the Z axis. The three curves track the position of central point of two sensors in local coordinate system during the translation. The central position on X axis varies form -0.1 inch to +0.1 inch; The

Y data remains close to zero while only the X axis translation occurs. The Z axis measurement remains close to -0.152 inch which is the original distance between the magnet and sensors. However, the Z axis rotation shown in Figure 5.2(b) shows a larger error as high as 2 degrees while it should have remained at zero degrees.

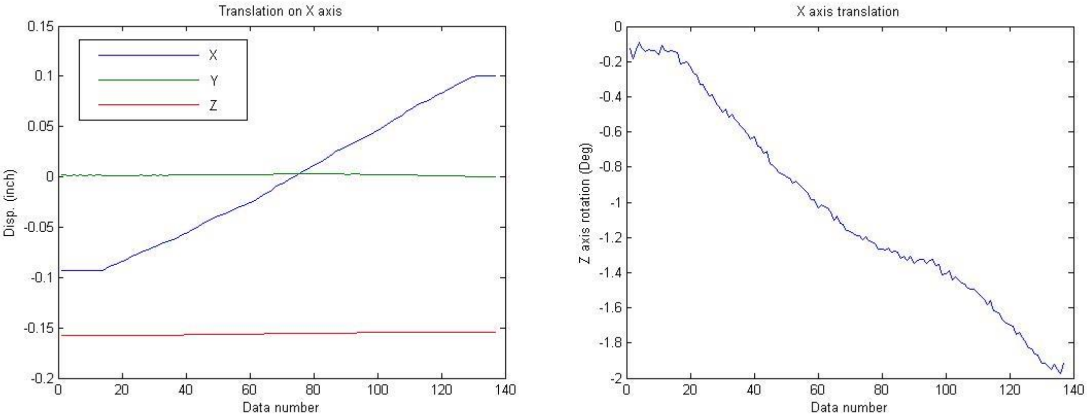

(a) X-Y-Z position

(b) Gamma

Figure 5.2: (a) X-Y-Z position and (b) Z axis rotation while translating along the X axis from -0.1 inch to +0.1 inch.

Figure 5.3(a) shows the magnet moving from -0.10 inch to +0.10 inch on the Y axis while fixing the X and Z axes and no rotation about the Z axis. The three calculated X-Y-Z displacement curves are very close to the actual data, however, the rotation data displayed in Figure 5.3 (b) has an error as high as 1.5 degrees which should have been zero degrees.

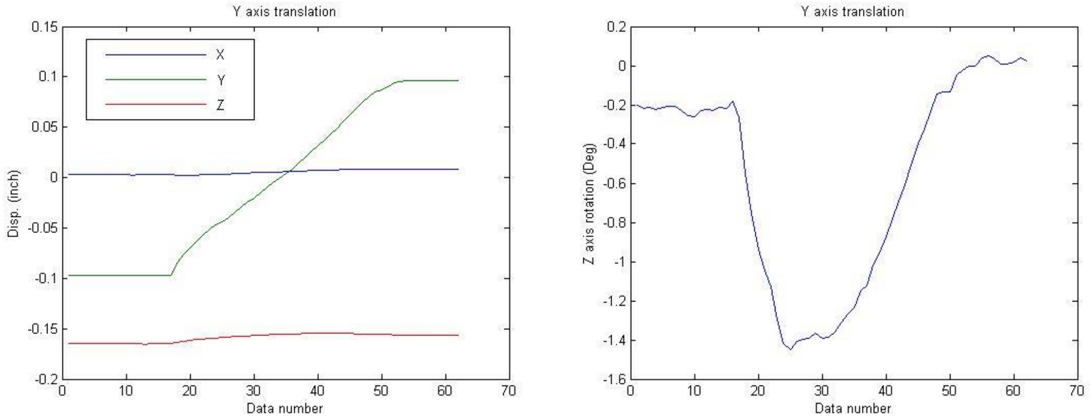

(a) X-Y-Z position *(b) Gamma*

Figure 5.3: (a) X-Y-Z position and (b) Z axis rotation while translating along the Y axis from -0.1 inch to +0.1 inch.

Figure 5.4 (a) shows the calculated X-Y-Z displacement moving the magnet from -0.172 inches along the Z axis in increments of 0.078 inches (2 mm) while the other three degrees of freedom are fixed. Here the data matches the expected results more closely. However, the Z axis rotation shown in Figure 5.4 (b) has a maximum error as high as 0.55 degrees.

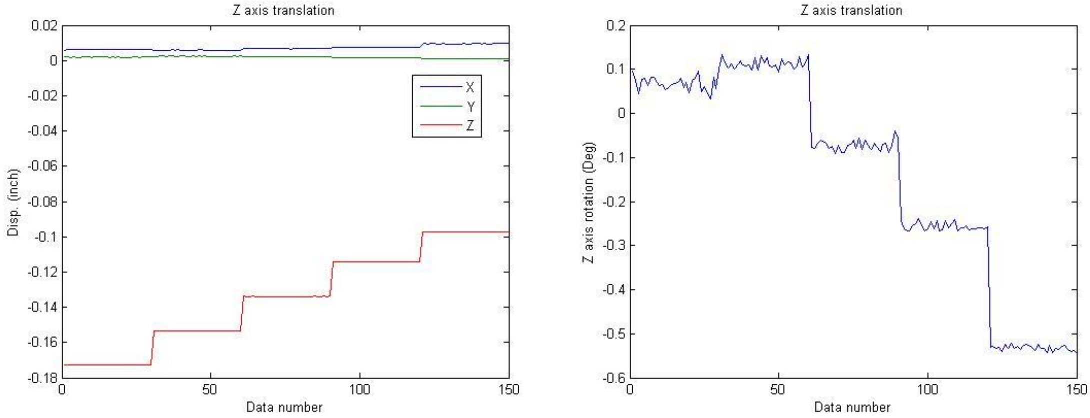

(a) X-Y-Z position (b) Gamma

Figure 5.4: (a) X-Y-Z position and (b) Z axis rotation during translation along Z axis

Figure 5.5(b) shows the calculated rotation angle gamma- γ rotating from -20 degree to +20 degree on the Z axis, which closely matches the actual data. In Figure 5.5(a), the crosstalk error on X-Y-Z displacement is as high as 0.01 inches. Recording the evaluation curves in Figure 5.2- Figure 5.5, the X-Y-Z position curves are close to actual data which demonstrates the feasibility of the localization method of magnet via the second set of analytic expression presented discussed in the Chapter 3. However, a calibration method is necessary to decrease error during real time 4-DOF combined load testing presented in Section 5.3.

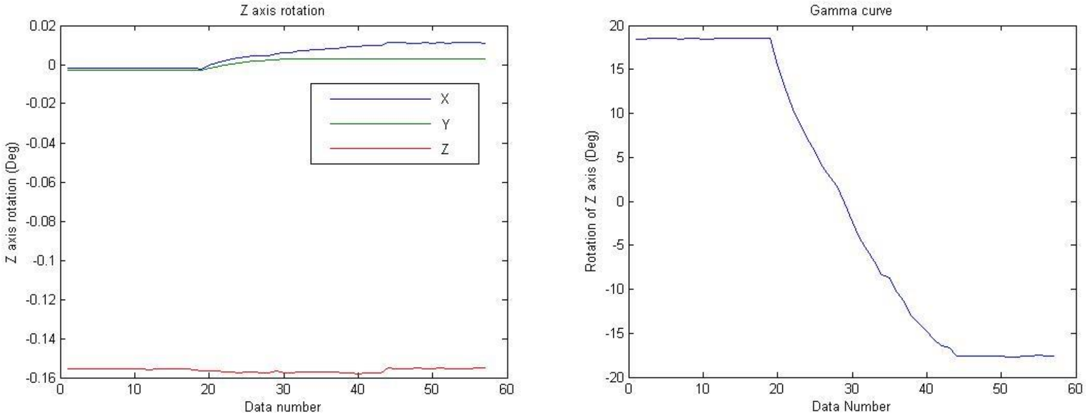

(a) X-Y-Z position

(b) Gamma

Figure 5.5: (a) X-Y-Z position and (b) Z axis rotation for rotation about the Z axis.

5.2 Single DOF Prototype Evaluation

To determine the linearity of prototype sensor, a single DOF evaluation is used the first set of analytic expressions to reveal the relationship between displacement of magnet and uniaxial loading on the sensor. To evaluate the prototype under uniaxial loading a tensile test machine (Instron 4411) was used. Two types of single DOF loading tests are performed - normal stress and shear stress.

5.2.1 Prototype Calibration

The two 3-axis Hall effect sensor detected the magnetic flux density (B_x, B_y and B_z) at the two sites. To determine the 3D spatial movement of the embedded magnet in the silicone (Dragon Skin Fx-Pro) under a combined loading a 3D data mapping was completed on a 3-axis micrometer stage. The magnetic flux density data (B_{x1}, B_{y1}, B_{z1}, B_{x2}, B_{y2}, B_{z2}) were processed using EUREQA as described in Chapter 3. The solution of three curve fitting analytic expressions F_1 , F_2 and F_3 presented in the Appendix for the position of the magnet on X, Y and Z axes were derived. In this work, the material is assumed to have linear and homogenous behavior and tests are performed at low strains.

5.2.2 Normal stress evaluation

In the normal loading testing (+Z axis), the prototype was subjected to a compressive load (300 N) across the top surface (2827 mm2) of the prototype. Loading on the prototype decreased the gap between the embedded magnet and the 3-axis Hall effect sensor. This resulted in a change in magnetic flux density measured by the Hall effect sensor. Figure 5.6 presents the normal stress by recording the displacement of the magnet on the Z axis. The magnitude of load is compared with the actual loading magnitude recorded from the tensile test machine load cell. In this experiment the maximum sensed normal force is 288.3N (102 kPa) which is close actual load of 300N (105 kPa) as recorded by the tensile machine. For the repeated tests shows linearity of the Hall effect sensor resulted in a coefficient of determination (RSQ) of 0.9996 for the averaged curve. The sensitivity of normal stress on Z axis is 1.12N/bit (0.397 kPa/bit). The linearity is very good as the coefficient of determination

(RSQ) is high as 0.9996. These results are for one configuration of the sensor and choice of material. The sensitivity can be adjusted with choice of elastomer stiffness and size of sensor.

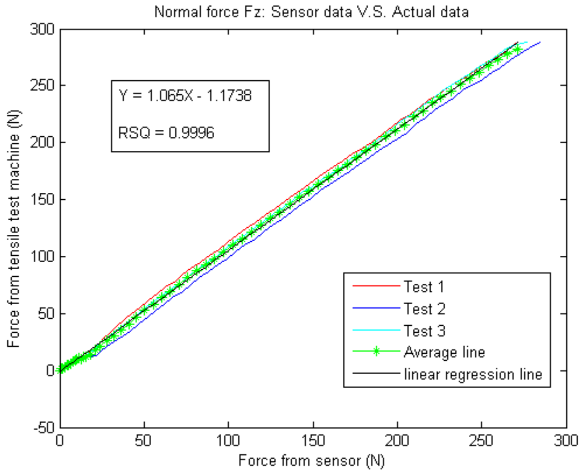

Figure 5.6: The evaluation of normal compressive loading in the Z axis

5.2.3 Shear stress evaluation

Figure 5.7 shows setup for the shear evaluation with the prototype assembled within a pair of holders, the top surface and the pedestal of the prototype were fixed on the two holders. The two holders were aligned through the center of the two holders to provide a relatively pure shear stress when the prototype is in tension. For this test, peak tension was set at 30 N and pull speed set at 3.00 mm per minute. The shear stress on the surface of prototype results in a horizontal movement of magnet, which leads to a greater change of magnetic flux density on X axis upon the 3D Hall sensor. In Figure 5.8 (a) and (b), the curves present shear stress along the X-axis. In addition, shear stress along the Y axis was also evaluated and presented in Figure 5.9 (a) and (b), respectively. The sensitivity of shear stress on X and Y axes is 0.099 N/bit (0.035 kPa/bit). The coefficient of determination (RSQ) is higher than 0.9994. Our choice of peak load (~10 kPa at 30 N) here is a result of the relatively soft material used and its adhesion to the substrate to avoid material delamination from the solid surfaces. Selection of material, sensors physical size, and fixation methods can adjust peak loading in shear and the resultant sensitivity accordingly.

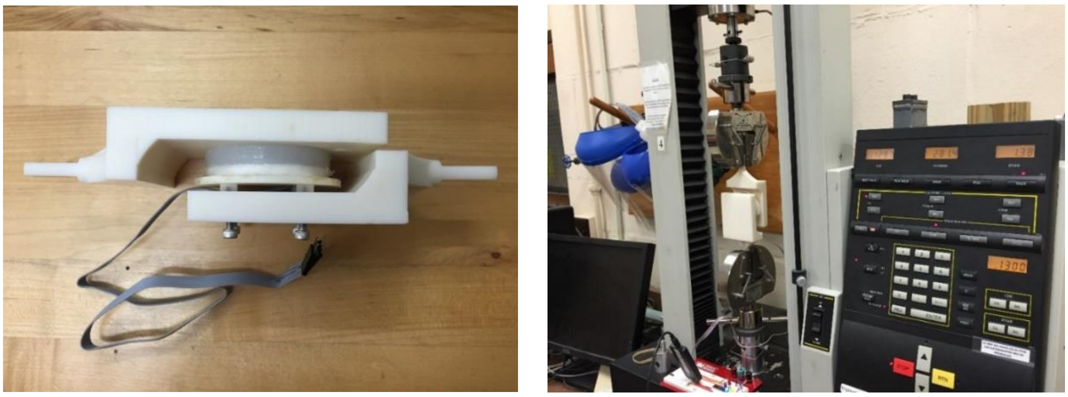

Figure 5.7: (left) Prototype is assembled with a pair of holders which are aligned through two pulling taps. (right) The initial prototype with a pair of holders is clamped on Instron 4411 for the shear stress test.

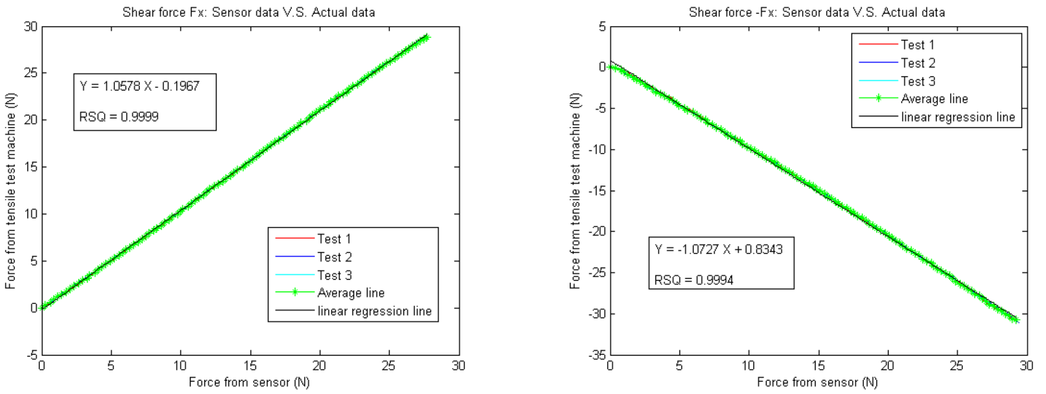

(a)

(b)

Figure 5.8: The evaluation of shear stress loading test on X axis: (a) positive direction; (b) negative direction

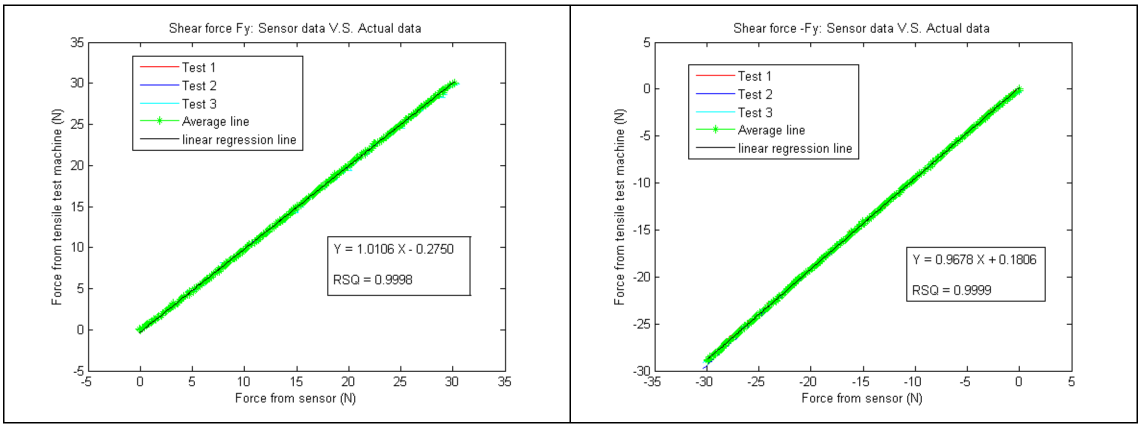

(a)	(b)

Figure 5.9: The evaluation of shear stress loading test on Y axis: (a) positive direction; (b) negative direction.

5.3 Real-time Prototype Evaluation under Combined Loading

In order to evaluate all the four degrees of freedom of the prototype sensor, a combined loading setup used a robotic arm (KUKA, LBR r820 iiwa) to evaluate the normal force, shear force and torque as shown in Figure 5.10. The internal torque sensors on the robotic joints were used to calculate the force in the X and Z axes and torque about the Z axis. The accuracy and precision test of root is accomplished through measuring gravity of a standard 1.5 Kg object. Based on linear performance on single degree of freedom evaluation, a linear calibration is also applied on this 4-DOF force and torque evaluation. Those linear calibration are determined by six set of combined loading, which are consisted of normal force in the Z axis, shear force in the X and Y axes and torque about Z axis. During the combined loading, a normal force is obtained by programing robot to push vertically on the prototype sensor. A torque applied in the Z axis is accomplished by programing robot to twist in the Z axis after applying the normal force. A shear force in the X axis is provided from a combined loading by programing robot to move along X axis after applying the torque. In order to obtain a shear force in the Y axis, the sensor is rotated by 90 degree then applied by the same combined loading for shear force in the Y axis. Finally, the 4-DOF measuring ability is evaluated under a combined loading test, which is composed of normal force, shear force and torque simultaneously. Considering crosstalk between each measuring components, a Square-Least multiple linear regression model was developed to improve accuracy of prototype sensor.

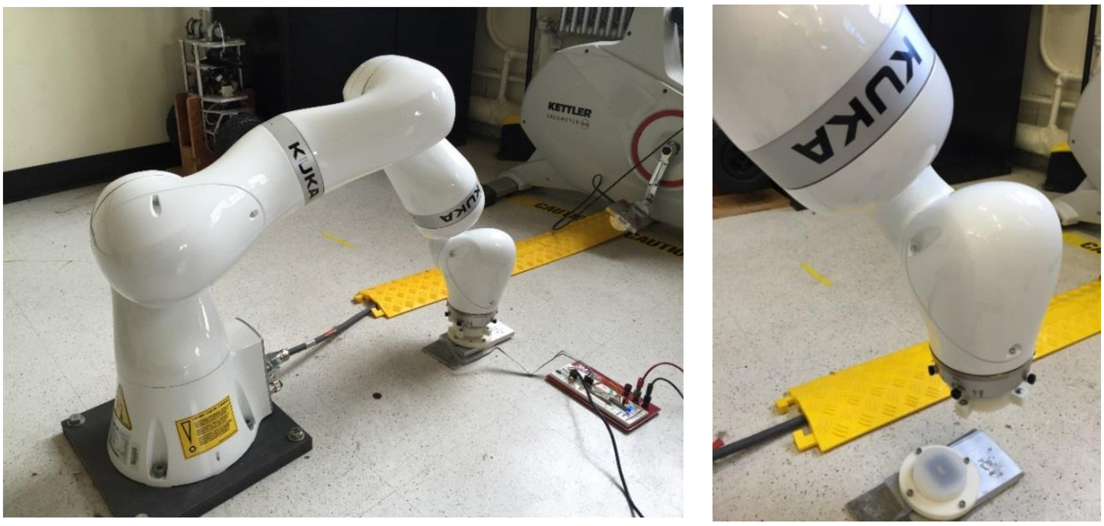

Figure 5.10: Robot arm applying combined loading to the prototype soft load cell.

5.3.1 Simple Linear Calibration of Force and torque

The robot was programed to measure the gravity of a standard 1.5 Kg object at ten different positions in the Z axis. Ignoring the dynamic error of robot, the accuracy and precision of robot was presented in the force curve, Figure 5.11. The average result is 12.0 N and standard deviation is 0.356 N, which means 2.90N offset exists but it is still a precise reference.

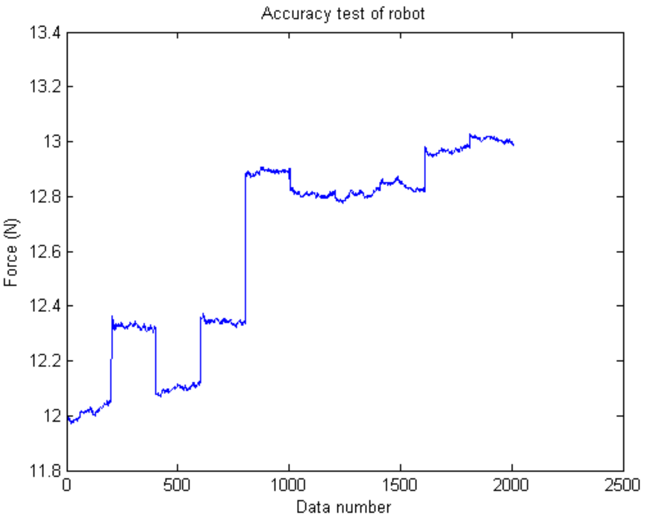

Figure 5.11: Accuracy and precision test of robot

In order to calibrated force and torque of prototype sensor, the robot is programed to apply two combined loading scenarios, which are repeated for three times as shown in Figure 5.12 and Figure 5.13. The first loading scenario is consisted of a normal force in the Z axis, F_z, shear force in the Y axis, F_y and a torque T_z about the Z axis. A normal force is accomplished by programing the robot to move in the Z axis for pushing the sensor vertically in increments of -10 N. The holding time between each step is 10 seconds and the maximum normal force is -40 N in compression. After the Z-axis force achieved -40 N in compression, the robot was programed to rotate on the Z axis at steps of 0.005 rad every 10 seconds and to increase the Z-axis torque T_z up to -0.8 N·m. Finally, the robot was programed to move on the Y axis at steps of 0.15 mm every 10 seconds and to decrease the -Y-axis force F_y by -15 N. In order to calibrate the shear force F_x, the second loading scenario was also applied for three times on prototype sensor with it rotated 90 degrees about the Z axis. The loading and torque curve is shown in last three data curve in Figure 5.12 and Figure 5.13.

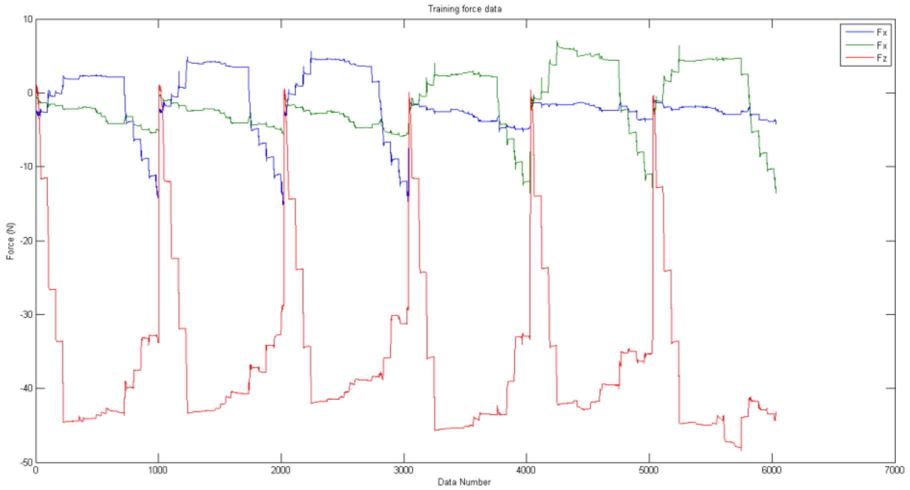

Figure 5.12: Force training data based on six set of combined loading

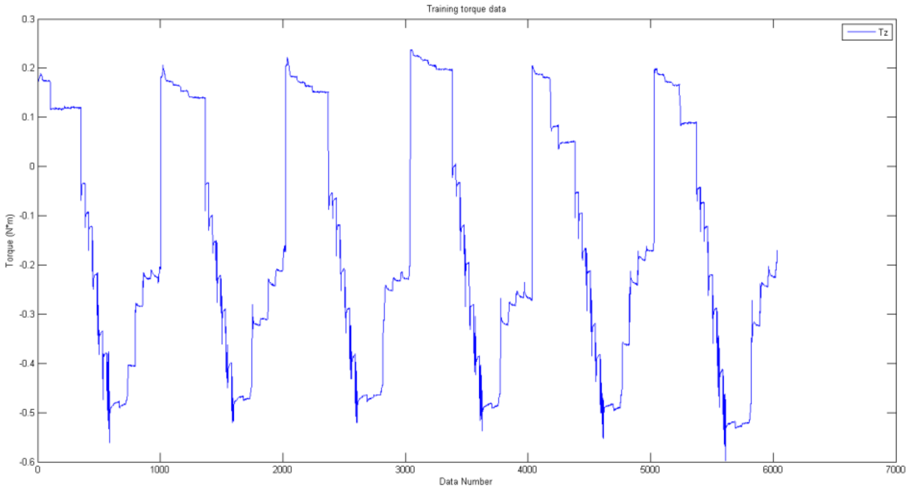

Figure 5.13: Torque training data based on six set of combined loading

The Least Square and Regression method is used to calibrate force and torque data. The principle of least squares was formulated by Karl Friedrich Gausse at the end of the 18th century to determine unknown parameters in mathematical model for minimize the sum of the squares of the differences between the actually observed and the computed values, multiplied by numbers that measure the degree of precision (34). Based on six dataset from the two combined loading scenarios, a simple linear calibration model (two parameters) is developed in Eqn. 33-36 , which calculate the force and torque only with variables of displacement z, y, x in the Z, Y and X axes and Z-axis rotation, θ. The coefficients of linear calibration for each DOF is obtained and present in Table 5.1.

$$\mathrm{F}_z(\mathrm{z}) = p1 * \mathrm{z} + p2 \tag{33}$$

$$\mathrm{F}_x(\mathrm{z}) = p1 * \mathrm{x} + p2 \tag{34}$$

$$\mathrm{F}_y(\mathrm{z}) = p1 * \mathrm{y} + p2 \tag{35}$$

$$\mathrm{T}_z(\mathrm{z}) = p1 * \theta + p2 \tag{36}$$

Table 5.1: Coefficients of linear calibration (two parameters model) on prototype sensor

	$p1$	$p2$
F_z	-233.5 N/mm	-837.8 N
F_x	27.23 N/mm	-3.727 N
F_y	28.34 N/mm	-5.921 N
T_z	-11.03 N·m/rad	0.5457 N

The combined loading scenario were repeated for two times and used to evaluate the two parameter linear calibrated readout from prototype sensor, which is rotated for 90 degree over the Z axis at the second time. In Figure 5.14, the linear calibrated force and torque is evaluated with the internal force and torque sensor. The absolute error between readout from sensor and robot is presented in Figure 5.14 (b) (d) (f)and (h). The average absolute error of normal force F_z is 4.4 N which is 11.0% of the full measurement range. The average absolute error of normal force F_x is 0.91 N which is 6.09% of the full measurement range. The average absolute error of normal force F_y is 0.51 N which is 3.40% of the full measurement range. The average absolute error of torque T_z is 0.09 N·m, which is 11.5% of the full measurement range. A spike is observed during shear force loading because of sudden impulses that occurred between the sensor and moving robot, which might be from internal sensor error in the robot. Another possible reason is that, the sample time of the prototype sensor is set as 0.2 second for capturing whole dataset from sensor in every cycle, which is much slower than robot. That long sample time might result in a too long response time to capture that sudden spike.

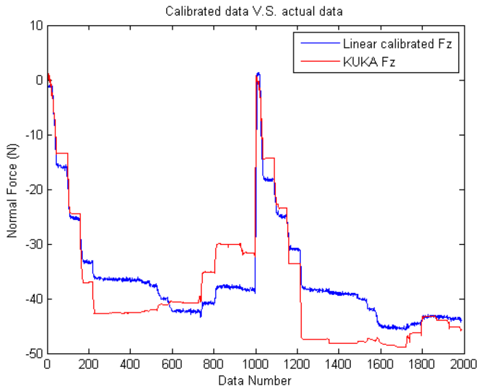
Calibrated data V.S. actual data
Linear calibrated Fz
KUKA Fz
Normal Force (N)
10
0
-10
-20
-30
-40
-50
0
200
400
600
800
1000
1200
1400
1600
1800
2000
Data Number

(a)

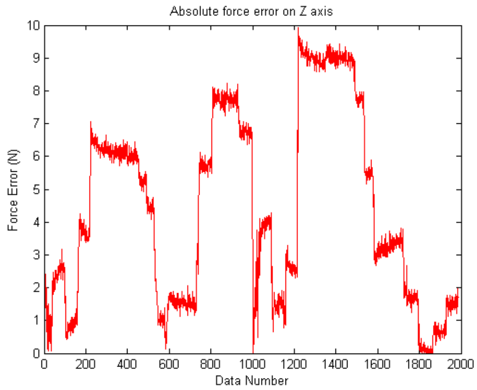
Absolute force error on Z axis
Force Error (N)
10
9
8
7
6
5
4
3
2
1
0
0
200
400
600
800
1000
1200
1400
1600
1800
2000
Data Number

(b)

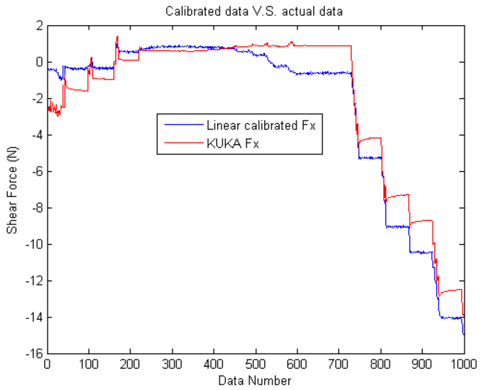
Calibrated data V.S. actual data
Linear calibrated Fx
KUKA Fx
Shear Force (N)
2
0
-2
-4
-6
-8
-10
-12
-14
-16
0
100
200
300
400
500
600
700
800
900
1000
Data Number

(c)

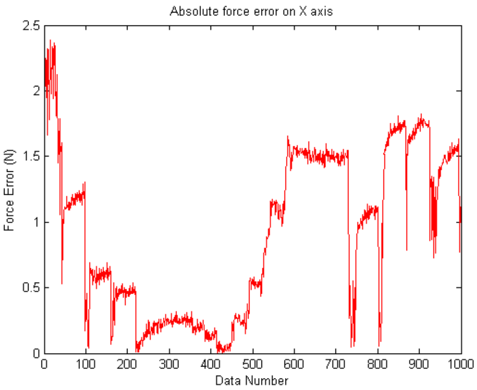
Absolute force error on X axis
Force Error (N)
2.5
2
1.5
1
0.5
0
0
100
200
300
400
500
600
700
800
900
1000
Data Number

(d)

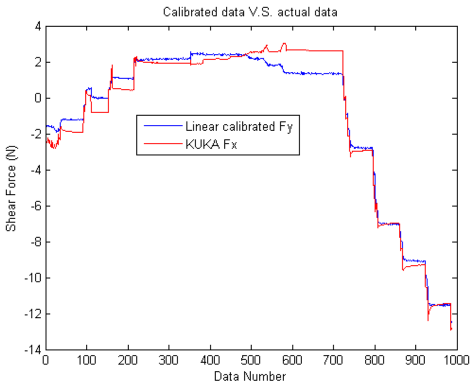
Calibrated data V.S. actual data
Linear calibrated Fy
KUKA Fx
Shear Force (N)
4
2
0
-2
-4
-6
-8
-10
-12
-14
0
100
200
300
400
500
600
700
800
900
1000
Data Number

(e)

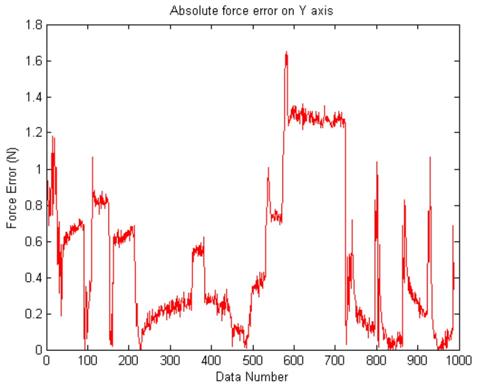
Absolute force error on Y axis
Force Error (N)
1.8
1.6
1.4
1.2
1
0.8
0.6
0.4
0.2
0
0
100
200
300
400
500
600
700
800
900
1000
Data Number

(f)

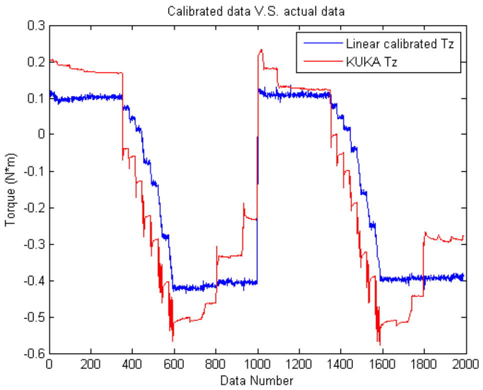
Calibrated data V.S. actual data
Linear calibrated Tz
KUKA Tz
Torque (N*m)
0.3
0.2
0.1
0
-0.1
-0.2
-0.3
-0.4
-0.5
-0.6
0
200
400
600
800
1000
1200
1400
1600
1800
2000
Data Number

(g)

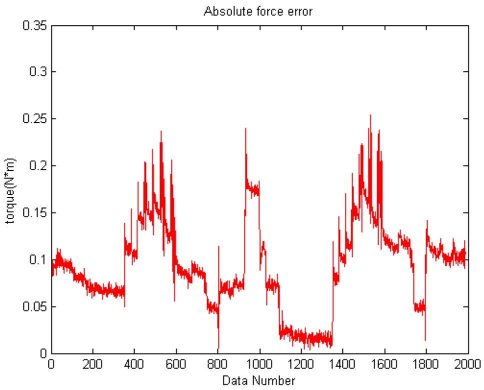
Absolute force error
torque(N*m)
0.35
0.3
0.25
0.2
0.15
0.1
0.05
0
0
200
400
600
800
1000
1200
1400
1600
1800
2000
Data Number

(h)

Figure 5.14: Linear calibrated (two parameters)force and torque from sensor versus actual data from robotic arm (a) evaluation of normal force $\mathrm{F_z}$; (b) absolute error performance of $\mathrm{F_z}$ under two set of normal force from 0 N to -40N(compression); (c) evaluation of normal force $\mathrm{F_x}$; (d) absolute error performance of $\mathrm{F_x}$ under one set of shear force from 0 N to -15N; (e) evaluation of normal force $\mathrm{F_y}$; (f) absolute error performance of $\mathrm{F_y}$ under one set of shear force from 0 N to -15N; (g) evaluation of normal force $\mathrm{T_z}$; (h) absolute error performance of $\mathrm{T_z}$ under two set of Torque from 0 N·m to 0.8 N·m.

5.3.2 4-DOF Evaluation with a decoupled calibration method

In order to decrease the crosstalk between each DOF result, a Least Square multiple regression model (Five parameters)is applied here. A simple mathematical model written from Least-Square method present in Eqn. 37, where g is the observed variable, $\alpha_1^0, \alpha_2^0, \dots, \alpha_n^0$ are parameters to be determined and $\varphi_1, \varphi_2, \dots, \varphi_n$ are known functions. In this project, G is the observed force and torque from robot here (F_x, F_y, F_z, T_z), φ^T (x, y, z, θ, 1) is consisted of displacement on X, Y and Z axis of magnet, angle of rotation about the Z axis and a constant 1 for the offset. The loss function $V(\alpha, t)$ is present in Eqn. 39. The loss function can be written in Eqn. 42 with the notations in Eqn. 40 and 41. The function Eqn. 42 is used to determine the solution of Least Square problem, which answer is shown in Eqn. 43.

$$g\ (i) = \varphi_1(i)\alpha_1^0 + \varphi_2(i)\alpha_2^0 + \cdots + \varphi_n(i)\alpha_n^0 = \varphi^T(i)\alpha^0 \tag{37}$$

$$\varphi^T(i) = (\varphi_1(i)\ \varphi_2(i) \dots\ \varphi_n(i)) \tag{38}$$

$$V(\alpha, t) = \frac{1}{2}\sum_{i=1}^{t}(g(i) - \varphi^T(i)\alpha)^2 \tag{39}$$

$$G(t) = (g(1)\ \ g(2)\ \dots\ g(t))^T \tag{40}$$

$$\Phi(t) = \begin{pmatrix} \varphi^T(1) \\ \vdots \\ \varphi^T(t) \end{pmatrix} \tag{41}$$

$$\Phi^T\Phi\hat{\alpha} = \Phi^T G \tag{42}$$

$$\hat{\alpha} = \alpha = (\Phi^T\Phi)^{-1}\Phi^T G \tag{43}$$

The same combined loading scenario in Figure 5.12 and Figure 5.13 are used as observed force G to solve the decoupling matrix α. For keeping a relative same magnitude for variables of each DOF, the unit of displacement is converted into millimeter, the unit of angle is converted into radian. By using the answer in Eqn. 43, the decoupled matrix α is introduced in Table 5.2.

Table 5.2: The decoupled matrix α (5×4)

	F_x	F_y	F_z	T_z
X	27.9 N/mm	22.6 N/mm	-9.02 N/mm	-0.247 N·m/rad
Y	-7.41 N/mm	31.3 N/mm	-0.946 N/mm	-0.213 N·m/rad
Z	4.14 N/mm	-20.9 N/mm	-303 N/mm	-0.882 N·m/rad
θ	8.73 N/mm	41.8 N/mm	212 N/mm	-10.9 N·m/rad
1	-33.0 N	-18.5 N	-796 N	-1.96 N·m/rad

Observed in the decoupling matrix, $\alpha,$ the diagonal elements mean the primary variable for each DOF, which is mostly dominated than other DOF. However, force and torque are also affected by variables from other DOF. Especially, shear force F_y is significantly affected by torque. The calibration results with decoupling method are presented in Figure 5.15. The average error of normal force decreases to 2.77 N (6.93%) and 0.069 N·m (8.62%) for the torque. The average error of shear force in the X axis goes down to 0.646 N (4.31%) and 0.391N (2.61%) in the Y axis.

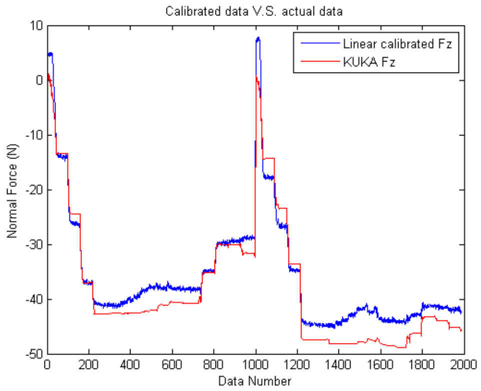
Calibrated data V.S. actual data
Linear calibrated Fz
KUKA Fz
Normal Force (N)
Data Number
10
0
-10
-20
-30
-40
-50
0
200
400
600
800
1000
1200
1400
1600
1800
2000

(a)

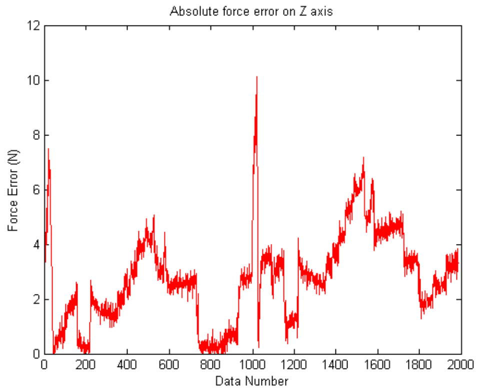
Absolute force error on Z axis
Force Error (N)
Data Number
12
10
8
6
4
2
0
0
200
400
600
800
1000
1200
1400
1600
1800
2000

(b)

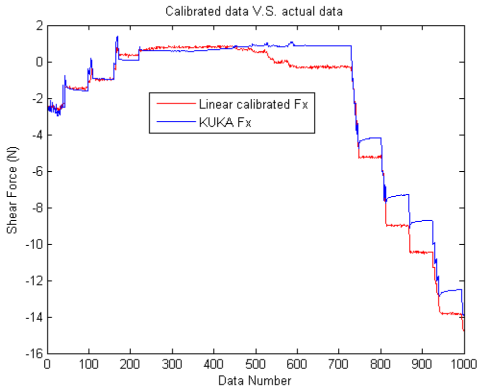
Calibrated data V.S. actual data
Linear calibrated Fx
KUKA Fx
Shear Force (N)
Data Number
2
0
-2
-4
-6
-8
-10
-12
-14
-16
0
100
200
300
400
500
600
700
800
900
1000

(c)

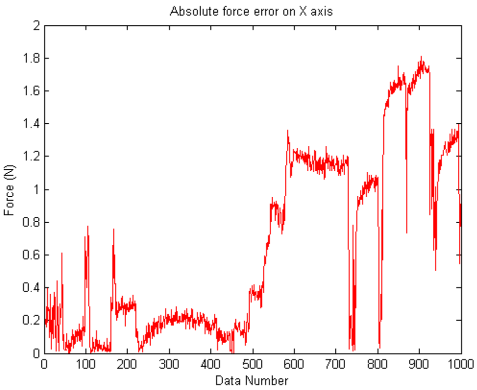
Absolute force error on X axis
Force (N)
Data Number
2
1.8
1.6
1.4
1.2
1
0.8
0.6
0.4
0.2
0
0
100
200
300
400
500
600
700
800
900
1000

(d)

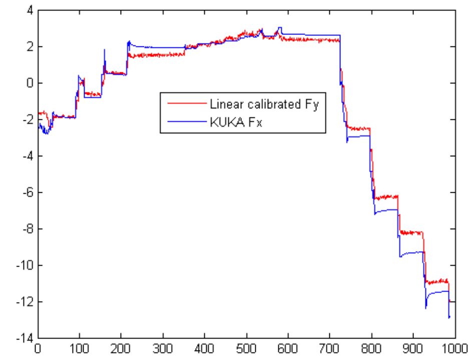
Linear calibrated Fy
KUKA Fx
4
2
0
-2
-4
-6
-8
-10
-12
-14
0
100
200
300
400
500
600
700
800
900
1000

(e)

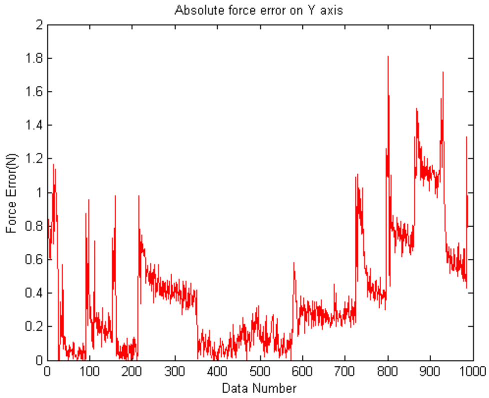
Absolute force error on Y axis
Force Error(N)
Data Number
2
1.8
1.6
1.4
1.2
1
0.8
0.6
0.4
0.2
0
0
100
200
300
400
500
600
700
800
900
1000

(f)

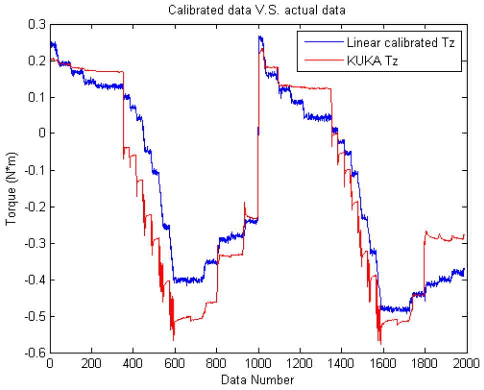
Calibrated data V.S. actual data
Linear calibrated Tz
KUKA Tz
Torque (N*m)
Data Number
0.3
0.2
0.1
0
-0.1
-0.2
-0.3
-0.4
-0.5
-0.6
0
200
400
600
800
1000
1200
1400
1600
1800
2000

(g)

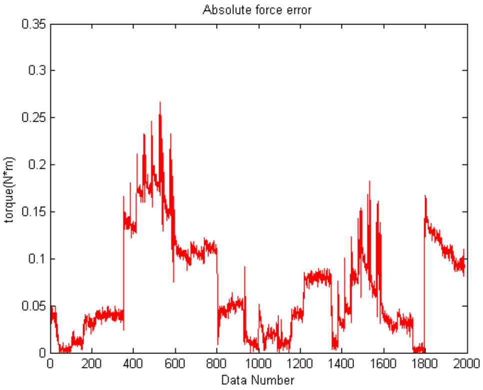
Absolute force error
torque(N*m)
Data Number
0.35
0.3
0.25
0.2
0.15
0.1
0.05
0
0
200
400
600
800
1000
1200
1400
1600
1800
2000

(h)

Figure 5.15: Linear calibrated (five parameters)force and torque from sensor versus actual data from robotic arm (a) evaluation of normal force F_z ; (b) absolute error performance of F_z under two set of normal force from 0 N to -40N(compression); (c) evaluation of normal force F_x ; (d) absolute error performance of F_x under one set of shear force from 0 N to -15N; (e) evaluation of normal force F_y ; (f) absolute error performance of F_y under one set of shear force from 0 N to -15N; (g) evaluation of normal force T_z ; (h) absolute error performance of T_z under two set of Torque from 0 N·m to 0.8 N·m.

Comparison results from two linear calibration methods (Two parameters and five parameters of Least Square Regression Model) are present in Table 5.3 - Table 5.4. Table 5.3 presents evaluation results of prototype sensor on normal force F_z, shear force F_x and F_y in the axis x and torque T_z by using two parameters linear calibration methods. By using the Least Square multiple regression model, the absolute averaged error of prototype sensor's performance decreases for all the DOF as shown in Table 5.4. The full measuring range for normal force is 40 N, 15 N for the shear force and 0.8 N·m for the torque. Observing from Table 5.3 and Table 5.4, the standard deviation also goes down for all the 4 DOF as well.

Table 5.3: Evaluation result of two parameters calibration on sensor under combined loading

	F_x	F_y	F_z	T_z
Abs average error	0.91 N	0.51 N	4.40 N	0.09 N·m
Error over the full range	6.09%	3.40%	11.0%	11.5%
Standard deviation	0.558 N	0.417 N	2.91 N	0.044 N·m

Table 5.4: Evaluation result of five parameters calibration on sensor under combined loading

	F_x	F_y	F_z	T_z
Abs average error	0.646 N	0.391 N	2.77 N	0.069 N·m

Error over the full range	4.31%	2.61%	6.93%	8.62%
Standard deviation	0.558 N	0.338 N	1.63 N	0.052 N·m

In conclusion, the 4 DOF measuring ability is proved by the combined loading evaluation applied by the robot. The calibrated result by using the Least Square multiple regression model (five parameters) shows more accurate performance than the simple Least Square regression model (two parameters). The reason caused error here might because of three parts: First, uneven contacting surface between sensor and robot produced a complicated loading scenario at very beginning of loading test. Secondly, the rotation of magnet over X and Y axis also occurred under the combined loading, which affected the accuracy of displacement and orientation of magnet. In addition, the material property of silicon used here is nonlinear performance, which is more complicated than linear performance assumed here. Therefore, the calibration method should be more complicated to shot for a higher precision for the prototype.

CHAPTER 6

CONCLUSION AND FUTURE WORK

In this project, a soft 4-DOF load cell was developed for robotic applications. The sensor is able to measure 4 degree of freedom load while maintain a soft exterior in a real interaction environment. The feasibility of the sensor, which owns characteristics of robust, low cost in components, light, compact and high loading capacity and low error, which were proved by real time loading test with the KUKA robotic arm that the prototype sensor is able to measure normal force up to 40 N, shear force up to 15 N and up to 0.8 N·m for torque on Z axis. The average relative error of full range for normal force is 6.9% of the full measuring range and 4.3% and 2.6% for shear force in the X and Y axes. The average relative error of torque over Z axis is 8.6%. The results show this is not a highly precise sensor, but its multi-axis capabilities, soft body, and slim form would be applicable to many robotic applications where a sense of force is important and not absolute measurements.

The error of the sensor is mainly caused by unexpected torque on the X and Y axes as result of potentially from loading errors using the KUKA robotic arm. In order to improve the accuracy of sensor, a more precise analytic expression of magnetic flux density should be determined. For solving the unexpected torque on the X and Y axes, a 6-DOF localization method discussed in Section 3.2 should be applied and the problem of expensive calculating time run by MATLAB also should be considered upon the complicated 6- DOF localization method.

In addition, selection for magnet and elastomer should be investigated further to resolve design trade-offs and be able to optimize the sensor for particular operating conditions such as loading capacity, resolution, response time and dimension for applying at different industrial environment. Finally, a more precise assembly and fabrication method should be implemented to reduce errors in the position and orientation placements for sensors and the magnet.

APPENDIX

ANALYTIC EXPRESSION DERIVED FROM EUREQA

FOMAT IN MATLAB CODE (Page 16)

%% First set of analytic expression

F_1= 4.21234964286322e-7*By2 + 0.216941974229745*atan(Bz1/Bz2) + 6.46515041037741e-7*By2^2/Bz1 + atan(1.35249016033068e-5*Bz1*Bx1/Bz2) - 0.160091902915269 - 1.78489857039123e-5*Bx1 - 1.30982794105611e-9*Bx1^2;

F_2 = 0.00372965181144634 + 2.01322714756875e-5*By2 + 1.02679845240304e-6*Bz1 + 8.68003045911792e-9*Bx1*By1 + 3.50187772957937e-9*Bz1*By1 + 0.205686661964569*atan((12.5751547328664 + 0.558673428914659*By2)/(Bx1 + 0.011353977882033*By1));

F_3= 4.32070672861422e-5*Bz2 + 3.99298953985811e-5*Bz1 + 3.99298953985811e-5*(By2^2)^cos(7.2323255099815e-5*Bx2)/Bz2 - 0.293631400754524 - atan(atan(6.82855529298458e-9*Bz1*Bz2 - 1.1371934027536e-5*Bx1)) - 5.78844001750442e-9*(By2^2)^cos(7.2323255099815e-5*Bx2);

FOMAT IN MATLAB CODE (Page 16)

%% Second set of analytic expression

% F_4 = 9.06781658776414e-5*Bx1 + 6.84987427279593e-5*Bz1 + 1.06034858885166e-7*By1^2 + -0.524050633021976*Bz1*Bx1/(9.35495384625777*By1 + 0.584869884476086*Bz1^2 + 0.000449267596572271*Bz1*By1^2 - Bz1*Bx1) - 0.0903644611316975;

% F_5 = 0.0487657973538183 + 3.64990725665809e-6*Bx1 + 0.179310634628595*atan(By1/(406.481600065323 - 1.06824850955514*Bx1)) - 4.96597311483188e-8*Bz1*By1 - 0.250656055634602*atan((1.68592095719576*By1 - 11.1455285824203)/(Bz1 - Bx1));

% F_6 = 1.06478109240017*(2.82880772542457e-7*By1^2 + 2.08019715244689e-7*Bz1^2 + -0.000233246140244451*Bx1^2/(Bx1 - Bz1))^0.118620278808138 - 0.92199384899376 - 7.29549960769636e-6*By1 - 8.76323941614347e-5*Bz1 - 6.73986754356789e-8*By1^2;

% F_7 = 9.73461549177479e-5*Bx2 + 0.278692006027524*atan(0.752918123340081*Bz2/Bx2) + 0.000173306165219446*By2*0.998727577710722^Bx2*(183.901014654467/Bz2)^(Bz2/Bx2)*atan(By2/Bz2) - 0.399962729613081 - 7.32118985611419e-5*Bz2;

% F_8 = 0.045573559445203 + 0.00521441715963551*By2/Bx2 + (95.018301243239*By2 - 1.61645451037815*Bx2)/(32639.2496420918 - Bz2^2 - 122.448952805785*Bz2 - 470.528920172616*Bx2 - 0.749132350220879*By2^2) - 6.72007031950879e-5*By2;

% F_9 = 8.35762760397241*cos(0.254666656401513 + 0.000445166761315684*Bz2 - 0.539647499537128*sqrt(0.000427442571331504*Bx2 + 1.24501406394539e-6*Bz2^2 + 3.19031369168088e-7*By2^2 + 16.4221791307586/(16.4221791307586 + Bx2) - 0.113824562076347)) - 8.4559235753169;

%

BIBLIOGRAPHY

1. *The intelligent ASIMO: System overview and integration.* Sakagami, Y., Watanabe, R., Aoyama, C., Matsunaga, S., Higaki, N., & Fujimura, K. . 2002, In Intelligent Robots and Systems, Vol. 3, pp. 2478-2483.

2. *Hippocrate: a safe robot arm for medical applications with force feedback.* Pierrot, F., Dombre, E., Dégoulange, E., Urbain, L., Caron, P., Boudet, S., ... & Mégnien, J. L. 3, s.l. : Medical Image Analysis, 1999, Vol. 3.

3. *Image-guided control of a robot for medical ultrasound.* Abolmaesumi, P., Salcudean, S. E., Zhu, W. H., Sirouspour, M. R., & DiMaio, S. P. 1, s.l. : IEEE Transactions on Robotics and Automation, 2002, Vol. 18.

4. *Development of robots for rehabilitation therapy: the Palo Alto VA/Stanford experience.* Burgar C G, Lum P S, Shor P C, et al. 2000, Journal of rehabilitation research and development, Vol. 37, pp. 663-674. 6.

5. *A small biped entertainment robot.* Kuroki, Y. s.l. : In Micromechatronics and Human Science, IEEE, 2001.

6. *Economics of robot application.* Dijkhuizen, A. A., Huirne, R. B. M., Harsh, S. B., & Gardner, R. W. . 1, s.l. : Computers and Electronics in Agriculture, 1997, Vol. 17.

7. *A soft multi-axis force sensor. In Sensors.* Vogt, D., Park, Y. L., & Wood, R. J. . s.l. : IEEE, 2012.

8. *A review of tactile sensing technologies with applications in biomedical.* Tiwana, M. I., Redmond, S. J., & Lovell, N. H. . s.l. : Sensors and Actuators A: physical, 2012, Vol. 179.

9. *Artificial sensing skin mimicking mechanoelectrical conversionproperties of human dermis.* D. De Rossi, A. Nannini, C. Domenici. 2, s.l. : IEEE Transactions on Biomedical Engineering, 1988, Vol. 35.

10. *Epidermis of human skin; pyroelectric and piezoelectric sensor layer.* H. Athenstaedt, H. Claussen, D. Schaper. 4549, s.l. : Science , 1982, Vol. 216.

11. *A Soft Multi-Axis Force Sensor.* Daniel Vogt, Yong-Lae Park and Robert J. Wood. s.l. : Sensors, 2012 IEEE, 2012.

12. *Tuning the sensing range and sensitivity of three axes tactile sensor using the polymer composite membrane.* C. Wen, W. Fang. s.l. : Sensors and Actuators A: Physical, 2008.

13. *Amicromachined active tactile senosr for hardness detection.* Y. Hasegawa, M. Shikida, T. Shimizu, T. Miyaji, H. Sasaki, K. Sato, K. Itoigawa. s.l. : Sensors and Actuators A: Physical , 2004.

14. R. Johansson, G. Leob, N. Wettels, D. Popovic, V. Santos. *Biomimetic tactile sensor for control of grip. 7,878,075* 2011.

15. *Polymer-based flexible tactile sensor up to 32 X 32 arrays integrated with interconnection terminals.* K. Kim, K. Lee, W. Kim, K. Park, T. Kim, J. Kim, J. Park. 2, s.l. : Sensors and Actuators A: Physical , 2009, Vol. 156.

16. *Normal and shear force measurement using a flexible polymer tactile sensor with embedded multiple capacitors.* Lee, H. K., Chung, J., Chang, S. I., & Yoon, E. 4, s.l. : Journal of Microelectromechanical Systems, 2008, Vol. 17.

17. *Design and Characterization of a Soft Multi-Axis Force Sensor Using Embedded Microfluidic Channels.* Daniel M. Vogt, Member. s.l. : IEEE Sensor journal, 2013, Vol. 13.

18. *Development of soft sensor exterior embedded with multi-aixs deformable tactile sensor system.* Asuka Kadowaki, Tomoaki Yoshikai, Marika Hayashi, Masayuki Inaba. s.l. : The 18th IEEE International Symposium on Robot and Human Interactive Communication, 2009.

19. *A novel self-decoupled four degree-of-freedom wrist force torque sensor.* Aiguo Song *, Juan Wu, Gang Qin, Weiyi Huang. s.l. : Measurement, 2007, Vol. 40.

20. *A flexible and highly sensitive strain-gauge sensor using reversible interlocking of nanofibres.* Pang, Changhyun, Gil-Yong Lee. 9, s.l. : Nature materials, 2012, Vol. 11.

21. *Triaxial force transducer for investigating stresses at the stump/socket interface.* Williams R B, Porter D, Roberts V C and Regan J F. 1, s.l. : Medical and Biological Engineering and Computing, 1992, Vol. 30.

22. *Application of Magnetic Type Tactile Sensor to Gripper.* Hiroyuki Nakamoto, Satoru Takenawa. s.l. : 2013 IEEE Workshop on Robotic Intelligence in Informationally Structured Space (RiiSS) , 2013.

23. *On a new action of the magnet on electric currents.* Hall, E. H. 3, s.l. : American Journal of Mathematics, 1879, Vol. 2.

24. *Position and level sensing using Hall-effect sensing technology.* Pepka, G. 1, s.l. : Sensor Review, 2007, Vol. 27.

25. *Development of the 6-axis force/moment sensor for an intelligent robot's gripper.* G.S. Kim, J.J. Park. s.l. : Sens. Actuator, 2005.

26. *Development of a small 6-axis force/moment sensor for robot's fingers.* Kim, G.S. 11, s.l. : Measurement Science and Technology, 2004, Vol. 15.

27. *Tactile Sensor on a Magnetic Basis Using Novel 3D Hall Sensor - First Prototypes and Results.* Ledermann, Christoph, and Sascha Wirges. . Costa Rica : INES 2013- IEEE 17th International Conference on Intelligent Engineering Systems, 2013.

28. *Design and Characterization of a Three-Axis Hall Effect-Based Soft Skin Sensor.* Tomo, T. P., Somlor, S., Schmitz, A., Jamone, L., Huang, W., Kristanto, H., & Sugano, S. s.l. : Sensors, 2016.

29. *Analytic Expression of Magnetic Field Distribution of Rectangular Permanent Magnets.* Xiao-Fan, Gou, Yang Yong, and Zheng Xiao-Jing. 3, s.l. : Applied Mathematics and Mechanics, 2004, Vol. 25.

30. *A six-dimensional magnetic localization algorithm for rectangular magnet objective based on a particle swarm optimizer.* W. Yang, C. Hu, M. Q.-H. Meng, S. Song, and H. Dai. 8, s.l. : IEEE Transactions on Magnetics, 2009, Vol. 45.

31. [book auth.] Warren C. Young Raymond J. Roark. *Formulas for stress and strain.* 7th. 2002, p. 64.

32. COMSOL Multiphysics- the platform for physics- based modeling and simulation. [Online] COMSOL Multiphysics. [Cited: 06 21, 2016.] http://www.comsol.com/comsol-multiphysics .

33. Fraden, Jacob. *Handbook of Modern Sensors: Physics, Designs, and Application.* s.l. : Springer, 2010.

34. Karl Joha Astrom, Bjorn Wittenmark. *Adaptive control.* New York : Dover Publications, Inc, 2008.

35. *Thick-film multiDOF force/torque sensor for wrist rehabilitation.* C. Jacq, B. Lüthi, T. Maeder, O. Lambercy, R. Gassert, P. Ryser. s.l. : Sensors and Actuators A: Physical, 2010.

36. *Design of Advanced Leg Module for Humanoid Design of Advanced Leg Module for Humanoid* . K. Kaneko, S. Kajita, F. Kanehim, K. Yokoi, K. Fujiwara, H. Hirukawa, T. Kawasaki,M. Hiram, and T. Isommi. s.l. : In Robotics and Automation, 2002. Proceedings. ICRA'02. IEEE International Conference, 2002, Vol. 1.

37. *Dexterous anthropomorphic robot hand with distributed tactile sensor: Gifu hand II.* Kawasaki, H., Komatsu, T., & Uchiyama, K. 3, s.l. : IEEWASME Tram. Mechotmnics, 2002, Vol. 7.

38. *Development of six-axis force/moment sensor for a humanoid robot's intelligent foot.* Kim, G.S. 2, s.l. : Sensors & Actuators: A Physical, 2008, Vol. 141.

39. Eureqa: The Virtual Data Scientist. [Online] NUTONIAN. [Cited: 06 21, 2016.] http://www.nutonian.com/products/eureqa/.

40. *Limits to Poisson's ratio in isotropic materials.* Mott, P. H., & Roland, C. M. 13, s.l. : Physical review B, 2009, Vol. 80.

41. *Pressure Sensor: State of the Art, Design, and Application for Robotic Hand.* Almassri, A. M., Wan Hasan, W. Z., Ahmad, S. A., Ishak, A. J., Ghazali, A. M., Talib, D. N., & Wada, C. . s.l. : Journal of Sensors, 2015.